



**BRNO UNIVERSITY OF TECHNOLOGY**

VYSOKÉ UČENÍ TECHNICKÉ V BRNĚ

**FACULTY OF MECHANICAL ENGINEERING**

FAKULTA STROJNÍHO INŽENÝRSTVÍ

**INSTITUTE OF SOLID MECHANICS, MECHATRONICS AND  
BIOMECHANICS**

ÚSTAV MECHANIKY TĚLES, MECHATRONIKY A BIOMECHANIKY

**ADVANCED MULTIAXIAL CRITERIA IN DUCTILE  
FRACTURE PREDICTION**

POKROČILÁ VÍCEOSÁ KRITÉRIA PŘI PREDIKCI TVÁRNÉHO PORUŠOVÁNÍ

**HABILITATION THESIS**

HABILITAČNÍ PRÁCE

**AUTHOR**

AUTOR PRÁCE

**Ing. František Šebek, Ph.D.**

**BRNO 2020**



# Abstrakt

Tvárné porušování je jedno z důležitých témat v různých odvětvích, jako je automobilní, námořní či energetický průmysl. Za jistých předpokladů bylo vyvinuto mnoho přístupů k řešení problémů spojených s tvárným porušováním. Tato práce se zaměřuje na propojení mikrostrukturního a fenomenologického modelování tvárného porušování při velkých plastických deformacích, pokojové teplotě a kvazi-statickém monotónním zatěžování. Komplexní podmínka plasticity závislá na třech invariantech napětí s deviátorově sdruženým zákonem tečení byla svázána s několika pokročilými kritérii tvárného porušení včetně jednoho původního. Modely byly nakalibrovány pro slitinu hliníku 2024-T351 a zaimplementovány do komerčního explicitního konečnoprvkového kódu Abaqusu s cílem aplikace na dva testy, které nebyly součástí kalibrační procedury. Toto prokázalo dobrou schopnost predikce vzniku trhliny a jejího šíření modelovaného pomocí techniky mazání prvků při víceosé napjatosti. Na závěr byly detailně prodiskutovány výsledky a shrnuty náměty pro další práci.

## Klíčová slova

Iniciace lomu, šíření trhliny, poškození, změkčení materiálu, smykový lom.



# Abstract

Ductile fracture is one of the key topics in various branches, like the automotive, maritime or energy industry. Many approaches to problems related to ductile fracture have been developed under certain assumptions. The present work focuses on bringing together the microstructural- and phenomenological-based ductile fracture modelling under large plastic deformations, room temperature and quasi-static monotonic loading. The complex yield criterion dependent on three stress invariants with deviatoric associated flow rule was coupled with several advanced ductile fracture criteria including one original. The models were calibrated for the aluminium alloy 2024-T351 and implemented within the Abaqus commercial explicit finite element code in order to be applied to the two tests, which were not covered within the calibration procedure. This demonstrated a good predictability of the cracking onset and its propagation modelled by the element deletion technique under the multiaxial stress state. The results were discussed in detail and topics of future work were summarized in the end.

# Keywords

Failure initiation, crack propagation, damage, material softening, slant fracture.



# Declaration of originality

I, Ing. František Šebek, Ph.D., hereby declare that I have written this habilitation thesis on my own. I also declare that I have fully cited and referenced all information and results that are not original to this work.

Brno, 04. 08. 2020

Ing. František Šebek, Ph.D.

# Acknowledgement

I would like to express my deepest gratitude to my wife, family, friends and last but not least to my colleagues who helped me to become who I am.



# Contents

<b>List of Figures</b>	<b>12</b>
<b>List of Tables</b>	<b>13</b>
<b>Nomenclature</b>	<b>15</b>
Latin symbols . . . . .	15
Greek symbols . . . . .	16
Mathematical notation . . . . .	17
<b>1 Introduction</b>	<b>19</b>
1.1 Background and motivation . . . . .	19
1.2 Ductile fracture modelling . . . . .	20
1.2.1 Criteria dependent on the first principal stress . . . . .	20
1.2.2 Criteria dependent on the stress triaxiality . . . . .	21
1.2.3 Criteria dependent on the stress triaxiality and normalized third invariant of deviatoric stress tensor . . . . .	23
1.2.4 Continuum damage mechanics . . . . .	25
1.3 Objectives of the study . . . . .	28
<b>2 Experimental campaign</b>	<b>29</b>
2.1 Investigated material . . . . .	29
2.2 Tension of smooth cylindrical specimen . . . . .	33
2.3 Tension of notched cylindrical specimens . . . . .	34
2.4 Compression of notched cylindrical specimen . . . . .	34
2.5 Tension of notched tubular specimen . . . . .	35
2.6 Torsion of notched tubular specimen . . . . .	36
<b>3 Material modelling</b>	<b>37</b>
3.1 Model of elasticity . . . . .	38
3.2 Model of plasticity . . . . .	38
3.2.1 Constitutive law . . . . .	38
3.2.2 Von Mises yield criterion with associated flow rule . . . . .	39
3.2.3 Kroon–Faleskog yield criterion with associated flow rule . . . . .	39
3.2.4 Bai–Wierzbicki yield criterion with deviatoric associated flow rule . . . . .	41
3.2.5 Comparison of calibrated yield criteria . . . . .	44
3.3 Model of damage . . . . .	47

---

3.4	Model of failure . . . . .	50
3.4.1	Extended Mohr–Coulomb criterion . . . . .	51
3.4.2	Lou–Huh criterion . . . . .	52
3.4.3	KHPS2 criterion . . . . .	53
3.4.4	Comparison of calibrated ductile fracture criteria . . . . .	54
<b>4</b>	<b>Application</b>	<b>57</b>
4.1	Small punch testing . . . . .	57
4.2	Three-point bending . . . . .	60
<b>5</b>	<b>Conclusions</b>	<b>65</b>
5.1	Future studies . . . . .	65
	<b>References</b>	<b>67</b>
	<b>Appendices</b>	<b>79</b>
<b>A</b>	<b>Stress state characterization</b>	<b>79</b>

# List of Figures

1.1	Two spaces with two ductile fracture criteria curved only in one of each (normalized third invariant of deviatoric stress tensor is used within both spaces) . . . . .	22
1.2	Criteria proposed by Bao and Wierzbicki and Johnson and Cook . . . . .	23
1.3	Fracture locus of criterion proposed by Xue [79, 80] . . . . .	27
2.1	Scatter in flow curves published by Bai et al. [95], Wierzbicki et al. [42], Seidt and Gilat [96], Papasidero et al. [97] and Xiao et al. (for the reference strain rate and room temperature) [98] . . . . .	30
2.2	Scatter in points used for the ductile fracture criteria calibration from [99] and published by Wierzbicki et al. [42], Seidt [100] and Papasidero et al. [97]	30
2.3	EBSD analysis for the two perpendicular cuts . . . . .	31
2.4	Results from the standard tensile tests in two perpendicular directions and post-mortem specimen from transverse direction showing minimum ellipticity [80, 101] . . . . .	31
2.5	Grain size distribution in the transverse direction . . . . .	33
2.6	Inverse pole figures for the aluminium alloy 2024-T351 . . . . .	33
2.7	Drawing and responses of standard tensile specimens [80] . . . . .	34
2.8	Drawing and responses of tensile notched cylindrical specimens [80] . . . . .	34
2.9	Drawing and responses of upsetting notched cylindrical specimens [51] . . . . .	35
2.10	Drawing and responses of tensile notched tubular specimens [80] . . . . .	35
2.11	Drawing and responses of torsional notched tubular specimens [80] . . . . .	36
3.1	Meshed specimens with highlighted crack initiation locations (not in scale)	37
3.2	Stress–strain curves and calibrated conventional multi-linear flow curve [80]	38
3.3	Calibrated Kroon–Faleskog yield criterion compared to the von Mises one [80]	41
3.4	Calibrated Bai–Wierzbicki yield criterion compared to the von Mises one [51]	43
3.5	Modified curvatures of calibrated yield criteria . . . . .	44
3.6	Responses for standard tension and all plasticity models considered [51] . . . . .	45
3.7	Responses for experiments and computations, except for the standard tension	46
3.8	Damage evolution and fitted non-linear law [132] . . . . .	48
3.9	Flow curve of matrix with resulting force responses [132] . . . . .	49
3.10	Evolutions of stress triaxiality and normalized third invariant of deviatoric stress tensor before the averaging . . . . .	49
3.11	Polynomial constitutive law fitted to the conventional flow curve . . . . .	52
3.12	Meaning of individual material constants of KHPS2 criterion . . . . .	54

---

3.13	Comparison of states of plane stress and cut-off stress triaxialities . . . . .	56
3.14	Calibrated ductile fracture criteria with the points used for fitting . . . . .	56
4.1	Small punch testing apparatus and responses from experiments (the final punch displacements are approximate) . . . . .	57
4.2	Mesh layout for the small punch test specimen . . . . .	58
4.3	Experimental and computational force responses for the small punch testing	58
4.4	Damage parameter fields compared to the experimental obtained micrographs	59
4.5	Drawing and responses of the three-point bending . . . . .	60
4.6	Fractured specimens after the three-point bending test [99] . . . . .	61
4.7	Assembly and detail of meshed notched block for the three-point bending .	62
4.8	Three-point bending force responses from computations and experiments .	62
4.9	Fracture surfaces from experiments compared to those obtained computa- tionally, where the field of damage parameter is displayed . . . . .	63
4.10	Field of horizontal strain component in percent obtained using the digital image correlation from the experiment compared to the numerical simulations	64
A.1	Geometrical representation of the stress state . . . . .	79
A.2	Graphical representation of the deviatoric stress state measures . . . . .	80

## List of Tables

2.1	Chemical composition of 2024-T351 [80] . . . . .	29
3.1	Elastic constants and specific mass utilized within computations . . . . .	38
3.2	Calibrated material constants for Kroon–Faleskog yield criterion [80] . . . . .	40
3.3	Calibrated material constants for Bai–Wierzbicki yield criterion [51] . . . . .	43
3.4	Deviations between the experiments and all plasticity models considered [51] . . . . .	45
3.5	Calibrated damage-related material constants [132] . . . . .	49
3.6	Points used for the ductile fracture criteria calibration . . . . .	50
3.7	Calibrated material constants for the extended Mohr–Coulomb criterion . . . . .	51
3.8	Calibrated material constants for the Lou–Huh criterion . . . . .	53
3.9	Calibrated material constants for the KHPS2 criterion [51] . . . . .	54
3.10	Deviations of points used for calibration from the calibrated fracture criteria . . . . .	55



# Nomenclature

## Latin symbols

$a$	material constant
$A_1, \dots, A_5$	material constants of model proposed by Bai and Wierzbicki
$B_1, \dots, B_6$	material constants of model proposed by Bao and Wierzbicki
$c_a, c_c, c_s, c_t, c_\eta$	material constants of model proposed by Bai and Wierzbicki
$C$	material constant
$C_1, \dots, C_4$	material constants of model proposed by Wierzbicki et al.
$C_L$	fixed material constant
$C_m$	material constant
$D$	damage parameter
$D_0$	damage initiation
$D_1, \dots, D_5$	material constants of model proposed by Johnson and Cook
$D_c$	critical damage parameter
$D_s$	microstructural damage parameter
$\dot{D}_s$	microstructural damage parameter rate
$E$	Young's modulus
$E_1, E_2$	material constants of model proposed by Bai and Wierzbicki
$\tilde{E}$	actual (degraded) modulus of elasticity
$f$	yield function
$f_1, \dots, f_3$	trigonometric functions
$F_1, \dots, F_3$	material constants of model proposed by Xue
$F_c$	force from computation
$F_e$	force from experiment
$G$	shear modulus
$G_1, \dots, G_6$	material constants of KHPS2 criterion
$H$	plastic modulus
$H_1, \dots, H_3$	material constants of Hosford–Coulomb criterion
$k$	yield correction function
$K$	strength coefficient
$L$	Lode parameter
$L_1, \dots, L_4$	material constants of model proposed by Lou et al.
$M_1, M_2$	material constants of extended Mohr–Coulomb criterion
$m$	material constant
$n$	strain hardening exponent

$p$	hydrostatic pressure
$p_{lim}$	limiting pressure
$q_1, q_2$	material constants of double damage curve
$Q^{-1}$	damping coefficient
$r$	radial coordinate of cylindrical coordinate system
$\underline{s}$	deviatoric stress tensor
$S_1, S_2$	material constants of model proposed by Lemaitre
$t$	time
$t_\varepsilon$	loading time
$T$	temperature
$T_h$	homologous temperature
$T_m$	melting temperature
$T_r$	room temperature
$w$	weakening function
$Y$	damage strain energy release rate
$z$	axial coordinate

## Greek symbols

$\alpha$	damage exponent
$\beta$	weakening exponent
$\gamma$	function of deviatoric stress tensor
$\varepsilon_D$	damage strain threshold
$\dot{\varepsilon}_0$	reference strain rate
$\bar{\varepsilon}_D$	equivalent plastic strain for a given loading path
$\bar{\varepsilon}_f$	fracture strain
$\tilde{\varepsilon}_p$	effective plastic strain
$\dot{\tilde{\varepsilon}}_p$	effective plastic strain rate
$\bar{\varepsilon}_p$	equivalent plastic strain
$\dot{\bar{\varepsilon}}_p$	equivalent plastic strain rate
$\underline{\dot{\varepsilon}}_p$	plastic strain rate tensor
$\Delta\bar{\varepsilon}_p$	equivalent plastic strain increment
$\hat{\varepsilon}_f$	fracture strain for a particular test
$\eta$	stress triaxiality
$\eta_0$	material constant (initial stress triaxiality)
$\eta_a$	average stress triaxiality
$\eta_c$	cut-off stress triaxiality
$\theta_A$	azimuth angle
$\theta_L$	Lode angle
$\bar{\theta}$	normalized Lode angle
$\kappa$	curvature
$\bar{\kappa}$	modified curvature
$\Delta\lambda$	plastic multiplier increment

$\mu$	material constant
$\nu$	Poisson's ratio
$\xi$	normalized third invariant of deviatoric stress tensor
$\xi_0$	material constant
$\xi_a$	average normalized third invariant of deviatoric stress tensor
$\varrho$	radial coordinate of spherical coordinate system
$\sigma$	stress
$\sigma_1 \geq \sigma_2 \geq \sigma_3$	principal stresses ordered according to the magnitude
$\sigma_I, \sigma_{II}, \sigma_{III}$	principal stresses not ordered according to the magnitude
$\sigma_m$	mean stress
$\sigma_{tr}$	trial stress
$\sigma_y$	yield stress
$\tilde{\sigma}$	effective stress (flow stress of matrix)
$\bar{\sigma}$	equivalent stress
$\bar{\sigma}_f$	fracture stress
$\underline{\sigma}$	stress tensor
$\varphi$	polar angle
$\chi$	material constant

## Mathematical notation

Only a selection is presented here as the majority of used mathematical notation should be clear from the context.

$\times$	multiplication
$\cdot$	dot product
$:$	double dot product
$  $	absolute value
$\langle \rangle$	Macaulay brackets



# 1 Introduction

## 1.1 Background and motivation

The ductile fracture has been an issue since the metal was employed in engineering applications, which is a long time ago. The investigations have begun since the plasticity theory was introduced, because the ductile failure is a result of plastic deformation. It registered an accelerated growth of attention with increasing computational power as it was the case in many other fields.

The failure predictions aim at increasing the safety of machine elements, optimizing the manufacturing processes or investigating the structure behaviour in accidents [1, 2]. The non-destructive testing has to be employed for inspections of parts, when the inner flaws occur, while the numerical simulations are an effective tool in predicting those discontinuities [3]. The manufacturing costs may decrease, when the metal forming operations are optimized [4]. Apart from the products, the tools may be analysed too [5]. On the other hand, the cracking may be optimized in the processes as machining [6] or cutting [7] as well, where it is intended. The computations may be useful when there is a shortage of available material or the material is vintage or hazardous, like irradiated [8]. The design of a new material and its application in various services, like the ballistic protection [9], may also be of the interest. Immediate cost saving is apparent, but future problems with liability may be avoided as well. Nevertheless, it should be noted that the numerical simulations cannot ever replace the experiments [10].

Another step forward was employment of the digital image correlation [11]. It is useful in the calibration as well as the verification stage [12]. It should be noted that the utilization is mainly in sheet metal applications with biaxial stress state and major strains observable on the material surface. Nevertheless, the cracks often initiate inside the material in many cases so another option has to be sought, such as the tomography [13].

The isotropic hardening is often utilized in ductile fracture, while it is usually insufficient for predicting the springback [14]. Apart from kinematic hardening, the directional distortional hardening may be employed [15]. Another approach may be the crystal plasticity [16, 17] or probabilistic modelling [18]. The modelling of plasticity is very important within ductile failure, but not reviewed in detail within the present thesis.

The finite element method is usually employed to solve the fracture-related problems by means of the element deletion technique. Nevertheless, this is not the only method used to simulate the crack initiation and propagation. There are another options like the node separation method [19], meshless method [20] or the extended finite element method [21].

The possibilities of ductile fracture modelling are addressed in detail within the following section.

## 1.2 Ductile fracture modelling

The macroscopic plastic (inelastic) deformation is the most often realized through the dislocation glide on a microscopic level in metals at room temperature. As a result, the material fails when the ductility is exhausted. Therefore, the equivalent plastic strain accumulated throughout the loading history has been acknowledged as the governing variable. The attention is further paid especially to the phenomenological ductile fracture criteria, also sometimes referred to as empirical, and continuum damage mechanics. However, there is a broader variety of options how to simulate the ductile failure, like using the porosity based models [22, 23, 24], cohesive zone models [25, 26], peridynamics [28] or the model proposed by Wilkins et al. [29].

### 1.2.1 Criteria dependent on the first principal stress

In the beginnings, it was realized that the ductility increases with increasing hydrostatic pressure [30]. Therefore, the first influence on the ductile fracture was attributed to the stress state conventionally represented by the first principal stress. Proposed criteria were quite simple and usually one-parametric.

Cockroft and Latham [31] proposed the criterion as

$$\int_0^{\bar{\varepsilon}_D} \bar{\sigma} \left\langle \frac{\sigma_1}{\bar{\sigma}} \right\rangle d\bar{\varepsilon}_p = C, \quad (1.1)$$

where  $\bar{\varepsilon}_D$  is the equivalent plastic strain for a given loading path,  $\bar{\sigma}$  is the equivalent stress,  $\sigma_1$  is the first (maximum) principal stress,  $\langle \rangle$  are the Macaulay brackets,  $C$  is the material constant (a critical value – when reached, the material fails) and  $\bar{\varepsilon}_p$  is the equivalent plastic strain defined as

$$\bar{\varepsilon}_p = \int_0^{t_\varepsilon} \sqrt{\frac{2}{3} (\dot{\underline{\varepsilon}}_p : \dot{\underline{\varepsilon}}_p)} dt, \quad (1.2)$$

where  $t_\varepsilon$  is the loading time,  $t$  is the time,  $:$  is the double dot product and  $\dot{\underline{\varepsilon}}_p$  is the plastic strain rate tensor. The equivalent plastic strain is a cumulative quantity, which can be understood as a sum of plastic strain increments over a loading time.

When compared to the previous criterion, Brozzo et al. [32] included the mean stress dependency in the criterion proposed by Cockroft and Latham [31] as

$$\int_0^{\bar{\varepsilon}_D} \frac{2\sigma_1}{3(\sigma_1 - \sigma_m)} d\bar{\varepsilon}_p = C, \quad (1.3)$$

where  $\sigma_m$  is the mean stress.

Later, Oh et al. [33] modified the criterion proposed by Cockroft and Latham [31] so the criterion became dimensionless as

$$\int_0^{\bar{\varepsilon}_D} \left\langle \frac{\sigma_1}{\bar{\sigma}} \right\rangle d\bar{\varepsilon}_p = C. \quad (1.4)$$

A similar criterion was proposed by Ko et al. [34] as

$$\int_0^{\bar{\varepsilon}_D} \frac{\sigma_1}{\bar{\sigma}} \left\langle 1 + 3 \frac{\sigma_m}{\bar{\sigma}} \right\rangle d\bar{\varepsilon}_p = C. \quad (1.5)$$

### 1.2.2 Criteria dependent on the stress triaxiality

Although the criterion proposed by Oh et al. [33] was dimensionless, the usage of stress triaxiality has started to prevail. More detailed stress state characterization is given in Appendix A. The stress triaxiality is defined as

$$\eta = \frac{\sigma_m}{\bar{\sigma}}. \quad (1.6)$$

Rice and Tracey [35] proposed a criterion, which is also grouped with models based on the void nucleation, coalescence and growth, such as the one proposed by McClintock [36], in the following form

$$\int_0^{\bar{\varepsilon}_D} 0.283e^{\frac{\sqrt{3}}{2}\eta} d\bar{\varepsilon}_p = C. \quad (1.7)$$

The criterion is, as all the previously introduced ones, independent of the normalized third invariant of deviatoric stress tensor, which is defined as

$$\xi = \frac{27 \det(\underline{s})}{2 \bar{\sigma}^3}, \quad (1.8)$$

where  $\underline{s}$  is the deviatoric stress tensor. Nevertheless, the criterion proposed by Rice and Tracey [35] becomes curved along the normalized third invariant of deviatoric stress tensor, when transformed into the space of that stress state measure and the ratio of the first principal stress to equivalent stress. The latter stress state measure was used by Oh et al. [33] for defining the criterion, which becomes curved along the normalized third invariant of deviatoric stress tensor, when transformed into the space of that stress state measure and stress triaxiality. The whole problem is illustrated in Fig. 1.1.

All the previously introduced criteria, apart from the one proposed by Rice and Tracey [35], have inherently a cut-off due to its mathematical formulation. It means that there is a value of the stress triaxiality, below which no crack initiates. This can be illustrated by a vertical boundary, as in the case of the criterion proposed by Oh et al. [33] in Fig. 1.1.

Later on, the concept of damage parameter has been used. It is defined as follows

$$D = \int_0^{\bar{\varepsilon}_D} \frac{1}{\bar{\varepsilon}_f} d\bar{\varepsilon}_p, \quad (1.9)$$

where  $\bar{\varepsilon}_f$  is the fracture strain. The fracture strain can be dependent, among the strain rate and temperature, on the stress triaxiality and normalized third invariant of deviatoric stress tensor. Then, the damage evolution is normalized on the contrary to the previously introduced criteria with a material constant  $C$ , which generally takes a value different from unity, whereas the damage parameter takes zero for the undamaged material and unity for then fully damaged material at the point of failure. The dependency of damage parameter on the equivalent plastic strain is linear in Eq. 1.9, but it can generally be non-linear.

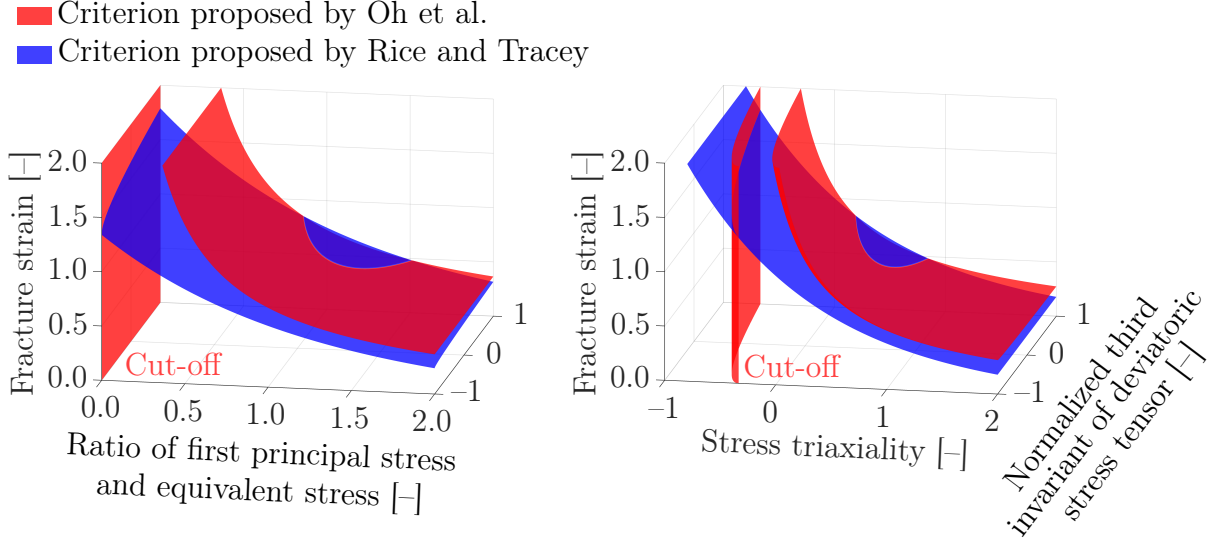


Figure 1.1: Two spaces with two ductile fracture criteria curved only in one of each (normalized third invariant of deviatoric stress tensor is used within both spaces)

Johnson and Cook [37] has proposed a criterion, which was actually first introduced by Johnson [38], depending on the stress triaxiality as

$$\bar{\varepsilon}_f = (D_1 + D_2 e^{D_3 \eta}) \left[ 1 + D_4 \ln \left( \frac{\dot{\varepsilon}_p}{\dot{\varepsilon}_0} \right) \right] (1 + D_5 T_h), \quad (1.10)$$

where  $D_1, \dots, D_5$  are the material constants,  $\dot{\varepsilon}_p$  is the equivalent plastic strain rate,  $\dot{\varepsilon}_0$  is the reference strain rate and  $T_h$  is the homologous temperature defined as

$$T_h = \frac{T - T_r}{T_m - T_r}, \quad (1.11)$$

where  $T$  is the temperature,  $T_r$  is the room temperature and  $T_m$  is the melting temperature. The criterion is dependent on the strain rate and temperature and is widely used in various applications requiring the consideration of these variables. It is illustrated in Fig. 1.2.

Bao and Wierzbicki [39], first published by Bao [40], conducted an extensive experimental program on aluminium alloy and found that the fracture strain dependency cannot be described by a simple decreasing function with increasing stress triaxiality. Therefore, the following expression was proposed

$$\bar{\varepsilon}_f = \begin{cases} B_1 (\eta + 1/3)^{B_2} & \text{if } -1/3 < \eta \leq 0 \\ B_3 \eta^2 - B_4 \eta + B_5 & \text{if } 0 < \eta \leq 0.4 \\ B_6 / \eta & \text{if } 0.4 < \eta \leq \infty \end{cases}, \quad (1.12)$$

where  $B_1, \dots, B_6$  are the material constants. The criterion is illustrated in Fig. 1.2. It was also concluded that there is a cut-off stress triaxiality  $\eta_c = -1/3$ , below which the damage parameter does not accumulate and therefore, there is no fracture. It is probably a correct assumption, but it was proved that the value is material dependent and can be lower than  $-1/3$  as initially thought. Finally, the complex dependency on the stress triaxiality was just one step before the Lode dependency was acknowledged. The dependency is called after Lode [27], who was among the first who described the effect of deviatoric stress state.

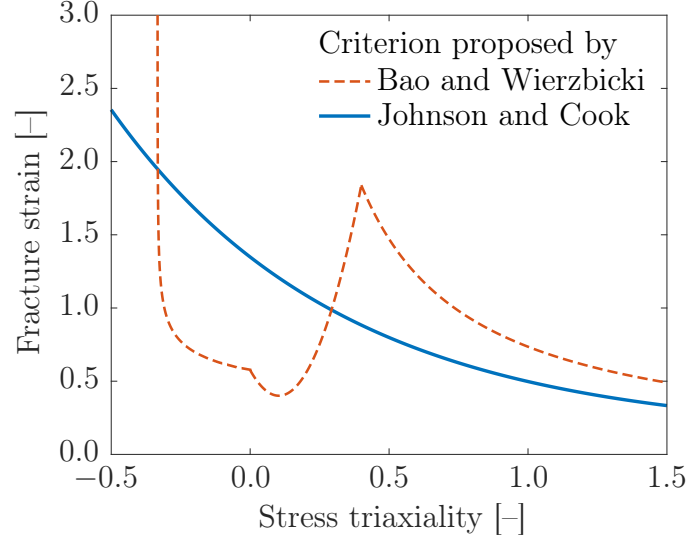


Figure 1.2: Criteria proposed by Bao and Wierzbicki and Johnson and Cook

### 1.2.3 Criteria dependent on the stress triaxiality and normalized third invariant of deviatoric stress tensor

Wilkins et al. [29] proposed a criterion depending not only on the hydrostatic pressure, but also on the deviatoric stress state assuming that the fracture strain decreased with increasing shear loading. Nevertheless, it took much longer before the Lode dependency has been widely accepted within the ductile fracture. Then, it even took its place within the porosity-based models [41]. Moreover, the lowest ductility at generalized shear also implies that the cut-off plane should be convex, which has not been much regarded in the literature yet. It will be further addressed accordingly.

Wierzbicki et al. [42] proposed a criterion dependent on the normalized third invariant of deviatoric stress tensor and stress triaxiality as

$$\bar{\varepsilon}_f = C_1 e^{-C_2 \eta} - (C_1 e^{-C_2 \eta} - C_3 e^{-C_4 \eta}) \left(1 - |\xi|^{\frac{1}{n}}\right)^n, \quad (1.13)$$

where  $C_1, \dots, C_4$  are the material constants,  $||$  is the absolute value and  $n$  is the strain hardening exponent. The fracture locus was symmetric with respect to the generalized shear.

Then, it was similarly followed by many others with asymmetric fracture loci. Bai and Wierzbicki [43] proposed a criterion, it was actually Bai [44] first, in a similar manner as

$$\begin{aligned} \bar{\varepsilon}_f = & \left[ \frac{1}{2} (A_1 e^{-A_2 \eta} + A_5 e^{-A_6 \eta}) - A_3 e^{-A_4 \eta} \right] \left[ 1 - \frac{2}{\pi} \arccos(\xi) \right]^2 \\ & + \frac{1}{2} (A_1 e^{-A_2 \eta} - A_5 e^{-A_6 \eta}) \left[ 1 - \frac{2}{\pi} \arccos(\xi) \right] + A_3 e^{-A_4 \eta}, \end{aligned} \quad (1.14)$$

where  $A_1, \dots, A_6$  are the material constants. It has not been widely used due to its unpredictable behaviour out of the calibrated range.

Nevertheless, Bai and Wierzbicki [45] later proposed more sophisticated (extended Mohr–Coulomb) criterion, it was Bai [44] first again, with a low number of material constants as

$$\begin{aligned} \bar{\varepsilon}_f = & \left[ \frac{K}{E_2} (1 - c_\eta [\eta - \eta_0]) \right. \\ & \times \left( c_s + \frac{\sqrt{3}}{2 - \sqrt{3}} (c_a - c_s) \left[ \sec \left( \frac{1}{3} \arcsin[\xi] \right) - 1 \right] \right) \\ & \left. \times \left( \sqrt{\frac{1 + E_1^2}{3}} \cos \left( \frac{1}{3} \arcsin[\xi] \right) + E_1 \left[ \eta + \frac{1}{3} \sin \left( \frac{1}{3} \arcsin[\xi] \right) \right] \right) \right]^{-\frac{1}{n}}, \end{aligned} \quad (1.15)$$

where  $\times$  is the multiplication sign,  $E_1$  and  $E_2$  are the material constants related to fracture,  $K$  is the strength coefficient (it comes from the Hollomon hardening law [46] together with  $n$ ), and finally the material constants from the slightly simplified yield criterion earlier introduced by Bai and Wierzbicki [43] as well:  $\eta_0$ ,  $c_\eta$ ,  $c_s$  and  $c_a$ , where

$$c_a = \begin{cases} c_c & \text{if } \xi < 0 \\ c_t & \text{if } \xi \geq 0 \end{cases}, \quad (1.16)$$

where  $c_c$  and  $c_t$  are the material constants. A slight modification will be presented within this thesis. Moreover, it simplifies into the following, when von Mises yield criterion is assumed

$$\begin{aligned} \bar{\varepsilon}_f = & \left[ \frac{K}{E_2} \left( \sqrt{\frac{1 + E_1^2}{3}} \cos \left( \frac{1}{3} \arcsin[\xi] \right) \right. \right. \\ & \left. \left. + E_1 \left[ \eta + \frac{1}{3} \sin \left( \frac{1}{3} \arcsin[\xi] \right) \right] \right) \right]^{-\frac{1}{n}}. \end{aligned} \quad (1.17)$$

Lou et al. [47] proposed a criterion for a sheet metal forming dependent on the stress triaxiality and maximum shear stress. Lou and Huh [48] developed an extension into the space of stress triaxiality and Lode parameter. Later, Lou et al. [49] introduced a changeable cut-off inspired by the criterion proposed by Cockroft and Latham [31], while all of this was actually first published by Lou [50] as

$$\begin{aligned} \bar{\varepsilon}_f = & L_3 \left( \frac{2}{\sqrt{3} [1 + \tan^2 (-\frac{1}{3} \arcsin[\xi])]} \right)^{-L_1} \\ & \times \left\langle \frac{1}{1 + C_L} \left( \eta + \frac{\sqrt{3} - \tan (-\frac{1}{3} \arcsin[\xi])}{3\sqrt{1 + \tan^2 (-\frac{1}{3} \arcsin[\xi])}} + C_L \right) \right\rangle^{-L_2}, \end{aligned} \quad (1.18)$$

where  $L_1, \dots, L_3$  are the material constants and  $C_L$  is the fixed material constant with a condition that  $C_L \neq -1$ . No constraint is needed for treating the cut-off plane shape as it is fixed.

A slight modification to this criterion was introduced by Kubík et al. [51] independently on and simultaneously with Xiao et al. [52]. It considered the fixed material constant ( $C_L$ ) as another material constant used for the fitting with implementing the constraint that  $\eta_c - \eta_a < 0$ , where  $\eta_a$  is the average stress triaxiality. Finally, Lou et al. [53] introduced another material constant into the cut-off in order to better govern the dependence on the deviatoric stress state measure. Although the material constants were already calibrated altogether, there was still prescribed a restriction on the cut-off stress triaxiality so that  $\eta_c = -2$  for  $\xi = -1$  (similarly done by Lou and Yoon [54] later). Therefore, the material constant can still be regarded as fixed, or semi-fixed, in such a case.

Roth and Mohr [55] proposed a (Hosford–Coulomb) criterion in a similar way as Bai and Wierzbicki [45] as

$$\bar{\varepsilon}_f = \left( \frac{K}{H_2} \left[ \left( \frac{1}{2} [(f_1 - f_2)^{H_1} + (f_2 - f_3)^{H_1} + (f_1 - f_3)^{H_1}] \right)^{\frac{1}{H_1}} + H_3(2\eta + f_1 + f_3) \right] \right)^{-\frac{1}{n}}, \quad (1.19)$$

where  $H_1, \dots, H_3$  are the material constants and  $f_1, \dots, f_3$  are the trigonometric functions dependent on the normalized third invariant of deviatoric stress tensor as

$$f_1 = \frac{2}{3} \cos \left[ \frac{1}{3} \arccos(\xi) \right], \quad (1.20)$$

$$f_2 = \frac{2}{3} \cos \left[ \frac{2}{3} \pi - \frac{1}{3} \arccos(\xi) \right], \quad (1.21)$$

$$f_3 = -\frac{2}{3} \cos \left[ \frac{1}{3} \pi - \frac{1}{3} \arccos(\xi) \right]. \quad (1.22)$$

#### 1.2.4 Continuum damage mechanics

The foundation of continuum damage mechanics was laid by Kachanov [56], who formulated the concept of effective stress and introduced the weakening function  $w$ , which is zero at the moment of fracture and unity for the undamaged material. Rabotnov [57] established a relationship between the weakening function and microstructural damage parameter as

$$w = 1 - D_s. \quad (1.23)$$

Then, the concept of effective stress (flow stress of matrix) is

$$\bar{\sigma} = \frac{\sigma}{1 - D_s}, \quad (1.24)$$

where  $\sigma$  is the stress.

Rousselier [58] proposed a model similar to Gurson's [59, 60, 61], but capable of the void growth in pure shear.

Krajcinovic and Fonseka [62] developed a constitutive equation for damaging brittle materials, which was later extended by Krajcinovic [63] to ductile materials as well.

Lemaitre [64, 65] formulated the coupling within the framework of the thermodynamics of irreversible processes and introduced the damage strain energy release rate as

$$-Y = \frac{\bar{\sigma}^2}{2E(1-D_s)^2} \left( \frac{2}{3}(1+\nu) + 3(1-2\nu)\eta^2 \right), \quad (1.25)$$

where  $E$  is the Young's modulus and  $\nu$  is the Poisson's ratio. The rate of microstructural damage parameter was defined as follows

$$\dot{D}_s = \begin{cases} 0 & \text{if } \tilde{\varepsilon}_p < \varepsilon_D \\ \frac{1}{1-D_s} \left( \frac{-Y}{S_1} \right)^{S_2} \dot{\tilde{\varepsilon}}_p & \text{if } \tilde{\varepsilon}_p \geq \varepsilon_D \end{cases}, \quad (1.26)$$

where  $\tilde{\varepsilon}_p$  is the effective plastic strain derived from the hypothesis of strain equivalence and  $\dot{\tilde{\varepsilon}}_p$  is its rate,  $S_1$  and  $S_2$  are the material constants and  $\varepsilon_D$  is the damage strain threshold. The material fails when  $D_s = D_c$  (not when  $D_s = 1$  as it should be according to Eq. 1.23), where  $D_c$  is the critical damage parameter which is another material constant. This approach has been followed by many others in various modifications [66, 67, 68, 69, 70].

Sidoroff [71] and Chaboche [72] introduced the anisotropic damage, for which Murakami and Ohno [73] proposed a procedure of symmetrizing the effective stress. Based on that, Chow and Wang [74] proposed an anisotropic model in the scope of Lemaitre's approach [64, 65], later followed within the thermodynamically consistent framework by others [75, 76, 77].

Kattan and Voyiadjis [78] decomposed the damage into two parts related to voids and cracks, respectively.

Xue [79] assumed that the flow stress of matrix is greater than the conventional flow stress of the material containing flaws, therefore

$$D_s \leq D. \quad (1.27)$$

In order to relate the micro and macro (Eq. 1.9) behaviour, Xue [79] introduced the weakening exponent  $\beta \geq 1$ , so

$$D_s = D^\beta. \quad (1.28)$$

Besides that, Xue [79] also proposed a nonlinear damage accumulation according to

$$D = \int_0^{\bar{\varepsilon}_D} \alpha \left( \frac{\bar{\varepsilon}_p}{\bar{\varepsilon}_f} \right)^{\alpha-1} \frac{d\bar{\varepsilon}_p}{\bar{\varepsilon}_f}, \quad (1.29)$$

where  $\alpha$  is the damage exponent.

Finally, Xue [79] also introduced a ductile fracture criterion in the following form

$$\bar{\varepsilon}_f = \tilde{\varepsilon}_f \left( 1 - F_1 \ln \left[ \frac{p}{p_{lim}} \right] \right) \left( F_2 + (1 - F_2) \left| \frac{6}{\pi} \theta_L - 1 \right|^{F_3} \right), \quad (1.30)$$

where  $\tilde{\varepsilon}_f$  is the fracture strain without confining pressure,  $p$  is the hydrostatic pressure,  $p_{lim}$  is the limiting pressure beyond which there is no fracture (cut-off),  $F_1, \dots, F_3$  are the material constants and  $\theta_L$  is the Lode angle defined on interval  $0 \leq \theta_L \leq \pi/3$  with respect to the normalized third invariant of deviatoric stress tensor as<sup>1</sup>

$$\xi = \cos(3\theta_L). \quad (1.31)$$

It should be noted that the fracture locus is symmetric (Fig. 1.3) as in the case of the criterion proposed by Wierzbicki et al. [42].

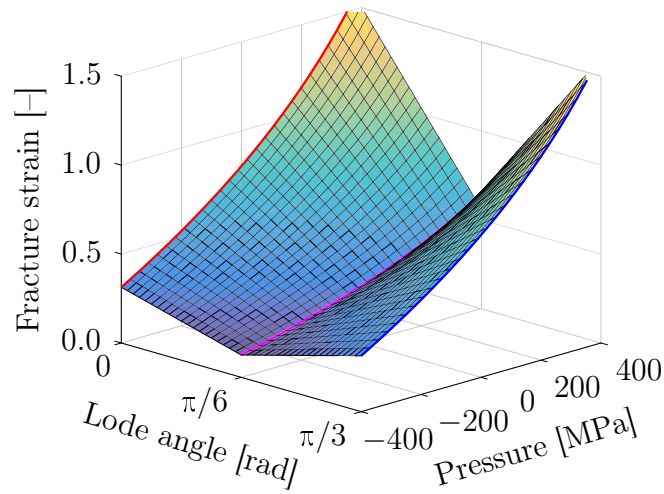


Figure 1.3: Fracture locus of criterion proposed by Xue [79, 80]

The so-called post-initiation softening is another technique, when the damage is partially coupled with elastic–plastic behaviour [81, 82, 83, 84, 85]. It means that the damage parameter accumulation is driven by the plastic deformation and in turn, the elastic behaviour and constitutive law is influenced by the amount of damage after some threshold. It was found challenging to produce the slant fracture with phenomenological ductile fracture criteria, which are uncoupled, from the previous three subsections. Therefore, the material weakening was introduced by the following formula

$$w = \left( \frac{D_c - D}{D_c - D_0} \right)^\chi, \quad (1.32)$$

where  $\chi$  is the material constant and  $D_0$  is the damage initiation, which is usually being equal to unity and when reached, the softening effect is triggered.

It should be noted that all the described solutions are mesh dependent. Moreover, the loss of ellipticity and subsequent localization occur when the coupled models are employed. This may be solved by the nonlocal regularization [86, 87, 88].

<sup>1</sup> More deviatoric stress state measures are described in Appendix A.

### 1.3 Objectives of the study

The objective of the present thesis is to study the ductile fracture modelling possibilities under the conditions of the monotonic quasi-static loading at room temperature. The main contributions may be summarized into a few bullets as:

- Estimate the elastic material behaviour using a reliable method.
- Estimate the constitutive law based on the standard tensile test.
- Design the experimental campaign with specimens geometries exhibiting the loading as close to proportional as possible.
- Calibrate the advanced yield criterion using the tests under various stress states.
- Calibrate the advanced ductile fracture criteria using a sufficient number of experiments.
- Apply the calibrated models to several tests to see the predictability.
- Assess the whole approach and propose the goals for the future studies.

## 2 Experimental campaign

### 2.1 Investigated material

The whole experimental campaign was carried out on the wrought aluminium alloy ČSN 42 4203<sup>2</sup> in the condition T351, hereinafter 2024-T351. The heat treatment designates that the material was solution heat-treated, stress-relieved and then naturally aged, while the stress relief was accomplished by the stretching of the metal by 1.5–3.0 % of deformation. There was no straightening after the stretching.

Although this aluminium alloy with the face-centred cubic structure does not exhibit an extensive necking, there have been conducted many tests in scope of ductile fracture [89, 90, 91]. Each batch is unique and the results may vary significantly. Flow curves from various sources are plotted in Fig. 2.1 with a huge scatter even in such a limited range. Moreover, the scatter in points for ductile fracture criteria calibration may be seen in Fig. 2.2. In order to avoid combining data from various sources like in [92, 93], and in order to eliminate the influence of microstructure or even misinterpreting the real material behaviour, the experimental campaign has been set up and the material was supplied by Ferropol as a cold-rolled plate with dimensions of  $1500 \times 1000 \times 20$  mm.

The chemical composition given in Table 2.1 is a result of three-times repeated measurement on Spectrumat GDS 750 obtained by the glow discharge optical emission spectroscopy.

Table 2.1: Chemical composition of 2024-T351 [80]

Element	Si	Fe	Cu	Mn	Mg	Cr	Zn	Ti	Ni	Pb	Sn
Composition [Weight %]	0.07	0.25	4.3	0.52	1.71	0.00	0.01	0.04	0.00	0.00	0.00

<sup>2</sup> Similar or equivalent designations are EN573 AW-2024, AW-AlCu4Mg1, AlCu4Mg1.5, AA2024, UNS A92024, AMS 4037, AL-P13, AlCuMg2, CG42, A-U4G1, AIR 9048-630, Wk.3.1355, LW3.1354, P-AlCu4.5MgMn, 9002/4, FA60-2024, A2024P, 1160, 2024, 3583, L-3140, BS 2L97, AMD2433, DTD5090, DTD 5100A or USA-WW-T-700/3 [94].

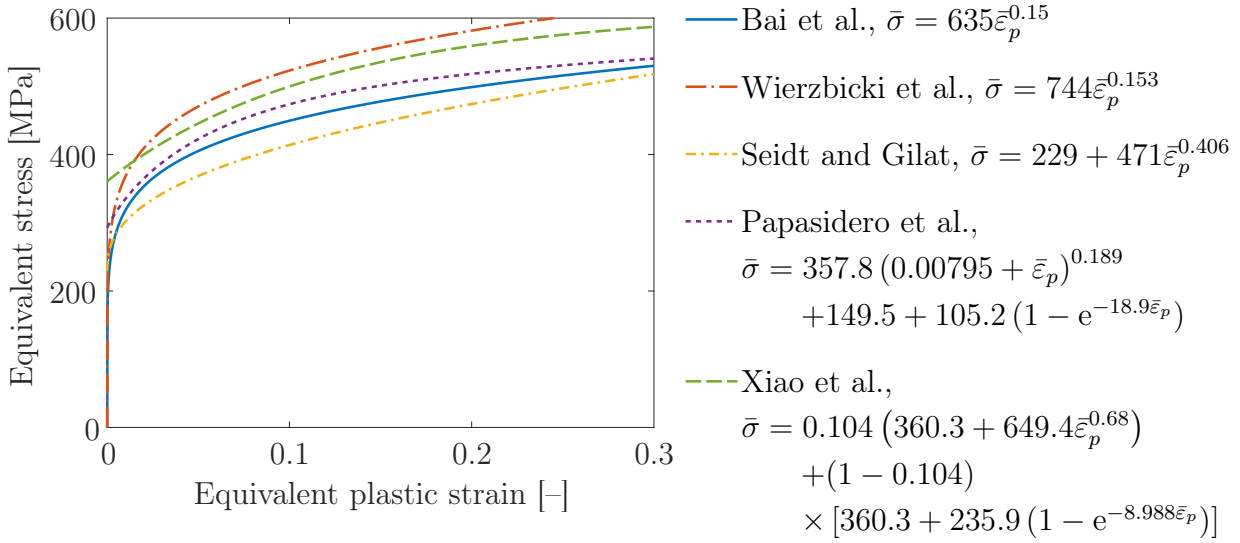


Figure 2.1: Scatter in flow curves published by Bai et al. [95], Wierzbicki et al. [42], Seidt and Gilat [96], Papasidero et al. [97] and Xiao et al. (for the reference strain rate and room temperature) [98]

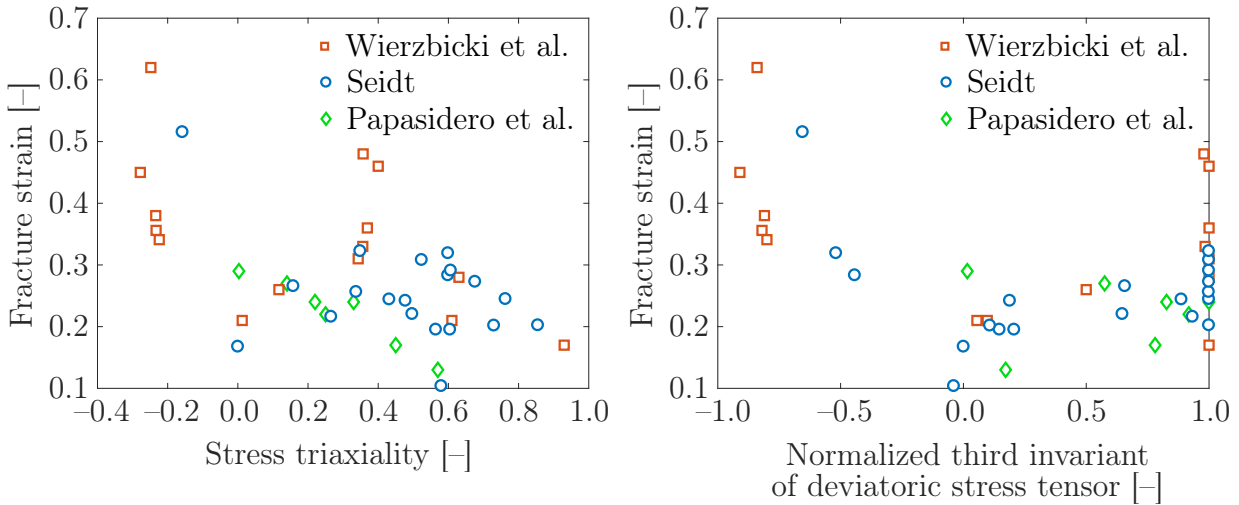


Figure 2.2: Scatter in points used for the ductile fracture criteria calibration from [99] and published by Wierzbicki et al. [42], Seidt [100] and Papasidero et al. [97]

The reference block of material was milled from the plate and the weight was measured using the analytical balance with 1 mg readability resulting in the density of  $2770 \text{ kg} \times \text{m}^{-3}$ . The block was used for non-destructive measurement of the wave velocity by the OLYMPUS 38DL PLUS ultrasonic thickness gauge with M110 contact transducer. The Poisson's ratio of 0.34 was computed knowing the Young's modulus (72500 MPa from the standard tensile tests conducted further) and average wave velocity of  $6347 \text{ m} \times \text{s}^{-1}$  [80].

Two metallographic specimens were hot pressed into the epoxy resin with a mineral filler (Struers DuroFast) on the ATM Opal X-Press, then grinded with sandpapers from SiC of P320, P500, P800, P1200, P2400 and P4000 roughness for three minutes, while water-cooled on the Struers Pedemin, mechanically polished using 3 and 1  $\mu\text{m}$  diamond paste and finally super-fine polished with OP-S suspension with ethanol wetting agent for three minutes per cycle. Then, the specimens were utilized for the analysis based on the Electron BackScatter Diffraction (EBSD). ZEISS Ultra Plus Scanning Electron Microscope (SEM) equipped with EBSD detector from the Oxford Instruments was deployed. The accelerating voltage of 20 kV was used, while the specimen was mounted at the angle of 70 degrees. The alloy was supplied as a cold-rolled product, so the size and orientation of grains suggest some anisotropy (Fig. 2.3).

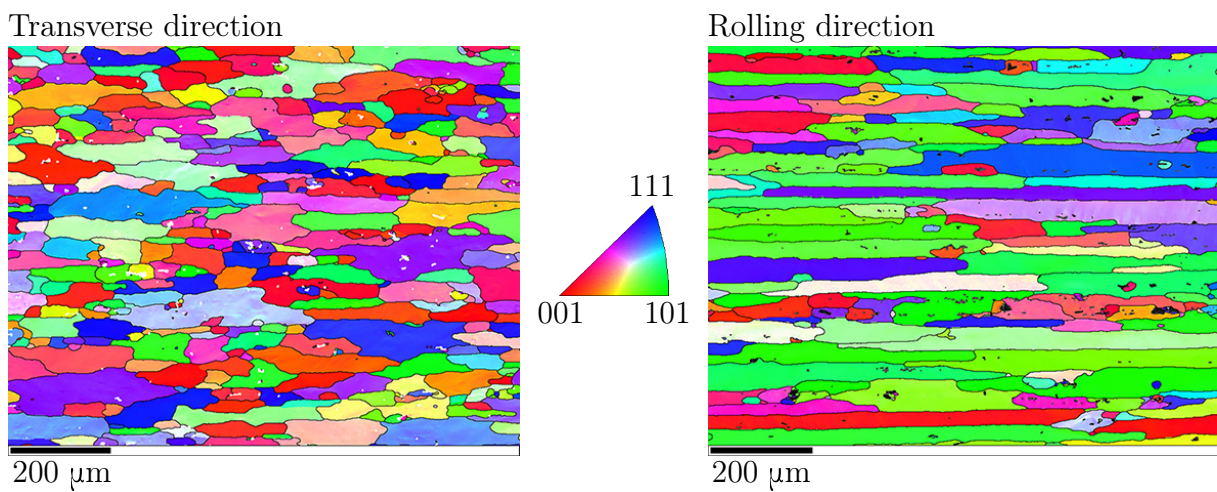


Figure 2.3: EBSD analysis for the two perpendicular cuts

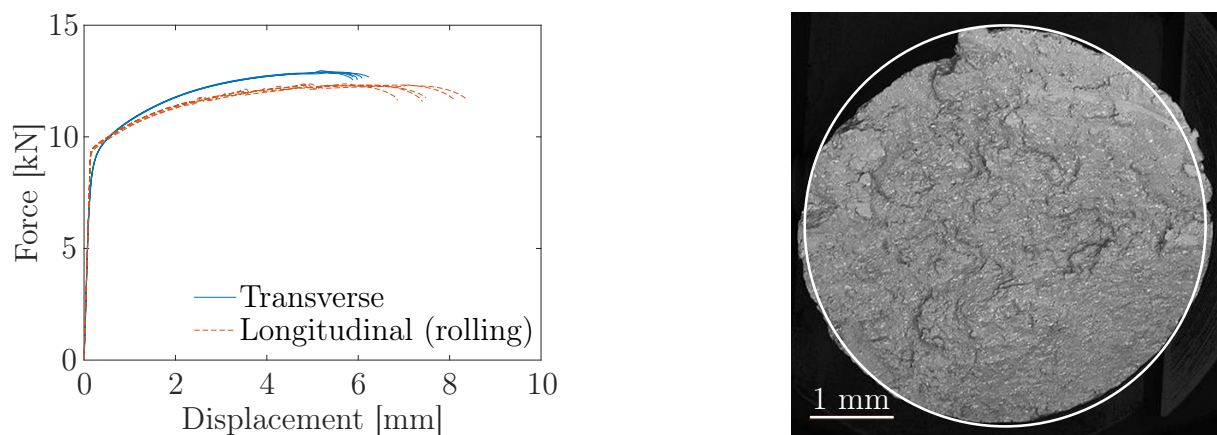


Figure 2.4: Results from the standard tensile tests in two perpendicular directions and post-mortem specimen from transverse direction showing minimum ellipticity [80, 101]

Nevertheless, the level of anisotropy was low in a macroscopic point of view in such a bulk material as demonstrated on the standard tensile tests as well as final shape of the post-mortem specimen from the transverse direction (Fig. 2.4), which was obtained using the SEM Tescan LYRA3 XMH [80, 101]. Therefore, the material was considered isotropic for the finite element modelling and all the specimens were manufactured having the axis parallel to the transverse direction, because there was only a minimum scatter in the displacements to fracture along that direction (Fig. 2.4) when compared to the longitudinal one. A minimum scatter in the force responses was then advantageously observed in the forthcoming tests as well. The influence of anisotropy would be smaller here than the scatter in results from the literature described in Figs. 2.1 and 2.2. The anisotropic yield criteria are, among other alternatives like the directional distortional hardening [15], another modelling approach to the one presented further, which could bring another issues. The anisotropic plasticity models are primarily utilized for the sheet metal forming, like stamping or deep drawing [102, 103]. It is possible to extend the proposed approach to cover the orthotropic behaviour, but it would mean for a bulk material that it becomes enormously complicated when the dependency on various stress invariants is introduced, it is very expensive when all the experiments are carried out for all the material directions (the number would be tripled), and it gives rise to the extensive number of material constants, making the final model inapplicable in practice or industry without any convincing improvement and clear physics behind it. Therefore, the assumption of isotropic behaviour was prioritized with the intention to use as complex up-to-date yield criterion as possible, yet simple to be calibrated, in order to accurately describe the whole variety of stress states neglecting a minor anisotropy. In conclusion, the assumption of 2024-T351 isotropy is supported by a number of other studies [92, 104, 105], which did not even employ any complex yield criterion. It is not typical to take the transverse direction for the ductile fracture analysis, but it should not play a significant role as long as the material was considered isotropic, therefore having all the global responses approximately identical in all directions. The presented microscopic observations represent only an informative content here, which are not directly reflected in the finite element modelling of homogeneous continuum using the phenomenological criteria. Unfortunately, such an information is often not given, which makes the analysis of published results difficult. For example, Bao and Wierzbicki [39] made an extensive analysis of 2024-T351 aluminium alloy, used across the ductile fracture community to these days [106]. Papisidero et al. [97] revisited these results and concluded that the disagreement with new own experiments should be accounted to the different microstructure, which brought no light into the topic as no information on the crystallographic texture was originally provided by Bao and Wierzbicki [39]. Besides that, there are studies paying attention to the influence of crystallographic texture on the fracture strains including the grain size level [107, 108, 109]. Finally, all the discrepancies may also be attributed to the gradually improving resolution of measuring devices and methods.

The grain size distribution is depicted in Fig. 2.5 for the transverse direction, while the inverse pole figures are in Fig. 2.6. Over 800000 data points were used for the EBSD analysis. The crystallographic texture exhibited a preferred orientation in crystallographic directions  $\langle 111 \rangle$  and  $\langle 101 \rangle$  parallel to the longitudinal direction, while crystallographic directions  $\langle 001 \rangle$  and  $\langle 111 \rangle$  parallel to transverse and width directions, respectively.

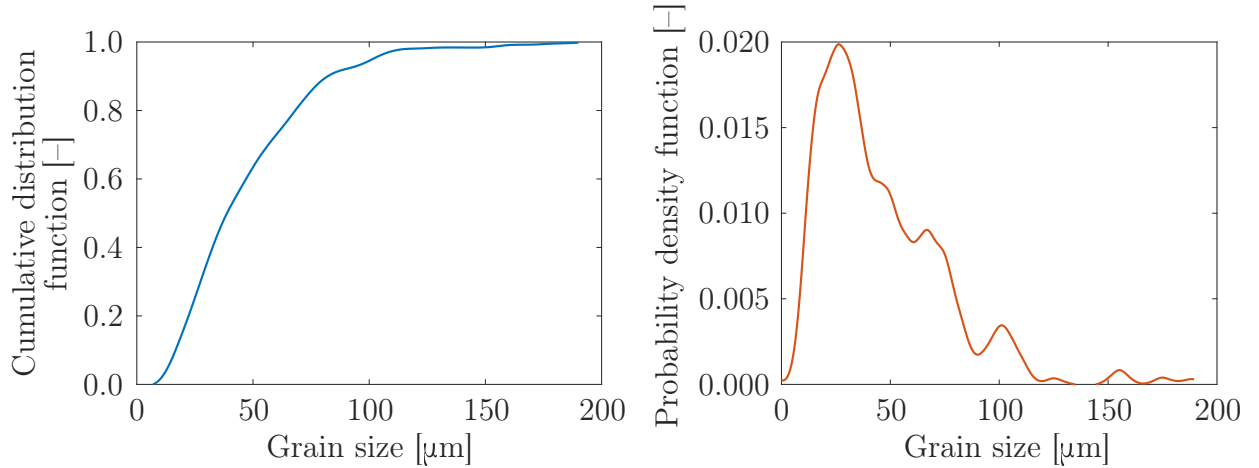


Figure 2.5: Grain size distribution in the transverse direction

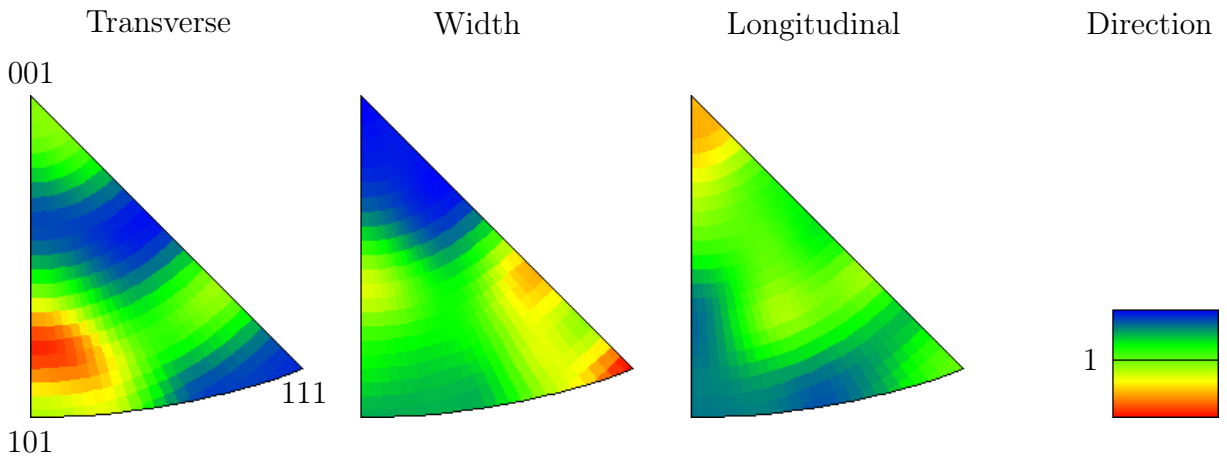


Figure 2.6: Inverse pole figures for the aluminium alloy 2024-T351

The crack initiated either on the specimens' surface or inside the specimens within this study, as discussed further. Nevertheless, all the specimens had the process zone, where the crack appeared sooner or later, prepared in the same quality. The surface roughness of  $0.4\mu\text{m}$  was prescribed on the detailed drawings, but much lower values between  $0.078$  and  $0.102\mu\text{m}$  were measured on a representative specimen using the BrukerContourGT-X8 Non-Contact 3D Optical Profiler. Therefore, the surfaces of process zones were prepared very carefully so that the surfaces roughness could not influence the results.

## 2.2 Tension of smooth cylindrical specimen

Five standard tensile tests were conducted on the Zwick Z250 Allround-Line, tCII, with the extensometer Zwick multiXtens of 30 mm gauge length. The specimens (Fig. 2.7) were pulled under the rate of 1 mm/min until the yield stress and then, the rate was smoothly increased to 2 mm/min [80]. The responses are displayed in Fig. 2.7.

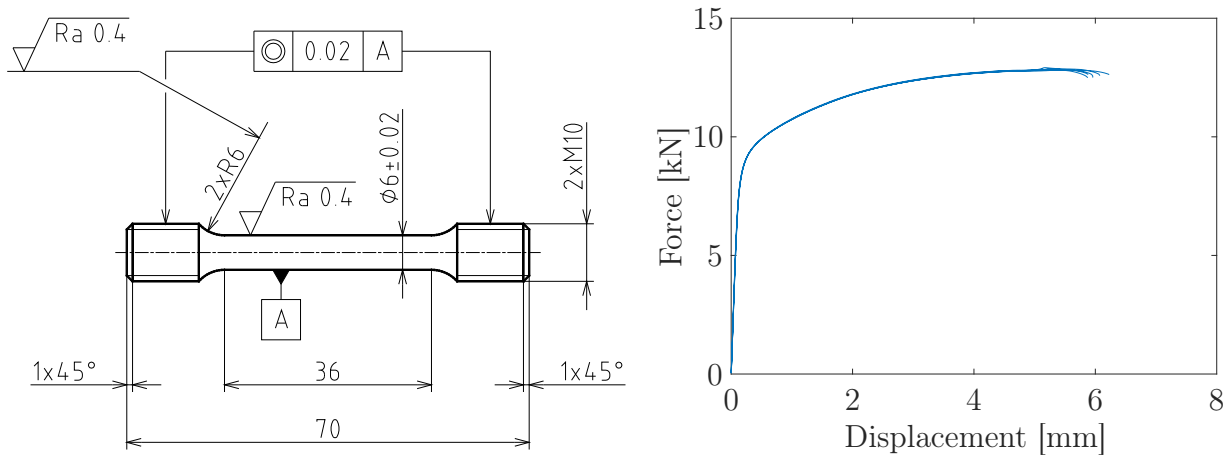


Figure 2.7: Drawing and responses of standard tensile specimens [80]

## 2.3 Tension of notched cylindrical specimens

Three tensile tests were conducted for each geometry depicted in Fig. 2.8 with notches R13, R6.5 and R4 (the latter two are not depicted in Fig. 2.8, but share the same geometry apart from the notch radii). Tests were carried out using the Zwick Z250 Allround-Line, tCII, and the extensometer Zwick multiXtens with a gauge length of 30 mm. The rate of 1 mm/min was used and the responses are in Fig. 2.8 [80].

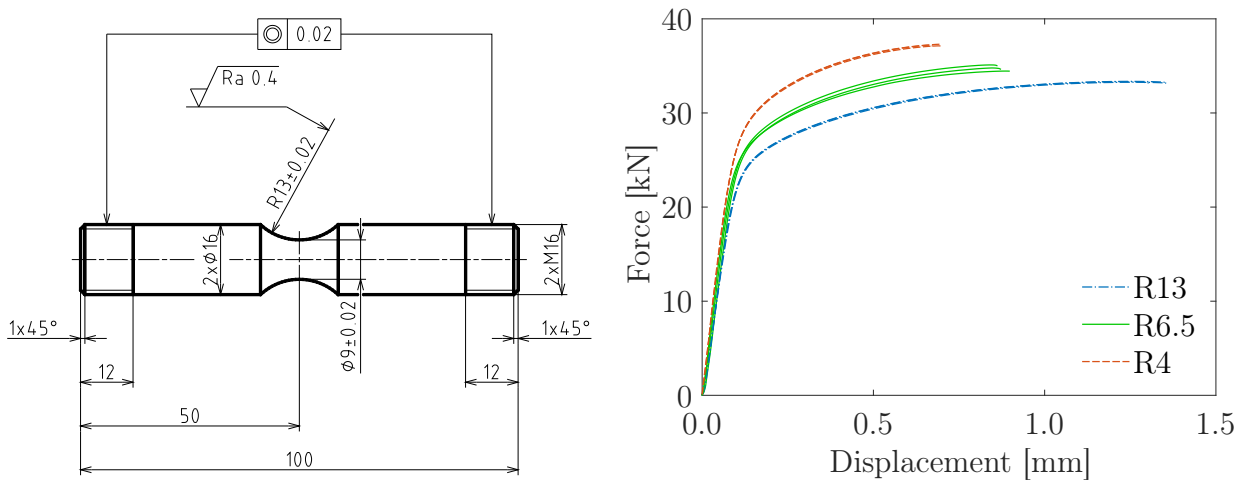


Figure 2.8: Drawing and responses of tensile notched cylindrical specimens [80]

## 2.4 Compression of notched cylindrical specimen

Two upsetting tests of notched cylindrical specimen were carried out (Fig. 2.9). Tests were realized using the Zwick Z250 Allround-Line, tCII, with the Zwick multiXtens extensometer following the compression. The rate of 1 mm/min was used. The responses are given in Fig. 2.9 [51].

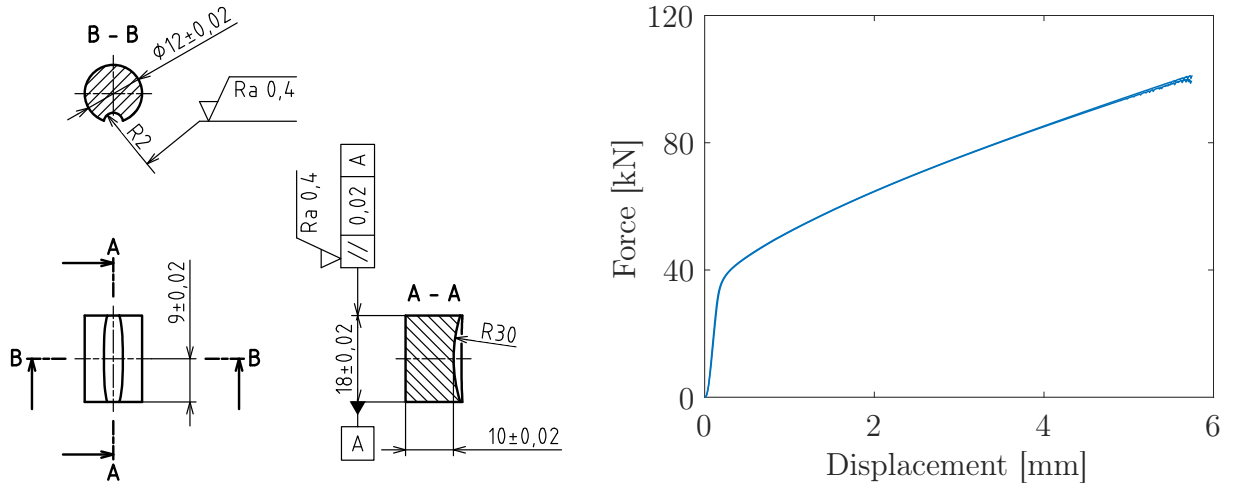


Figure 2.9: Drawing and responses of upsetting notched cylindrical specimens [51]

This new specimen geometry was designed, because the smooth compressed cylinder does not exhibit a clear crack initiation location. Moreover, the evolution of stress triaxiality and normalized third invariant of deviatoric stress tensor took from the surface in the middle of the specimen height, as usual, show high non-proportionality due to the barrelling [110, 111]. The aim of the present thesis is to have as proportional loading as possible, which will be presented further.

## 2.5 Tension of notched tubular specimen

Three tensile tests of notched tubular specimen (Fig. 2.10) were conducted on the Zwick Z250 Allround-Line, tCII, along with the Zwick multiXtens extensometer having 30 mm gauge length. The rate was 1 mm/min again. The responses are depicted in Fig. 2.10. Two universal joints were employed to prevent the misalignment of the specimen [80].

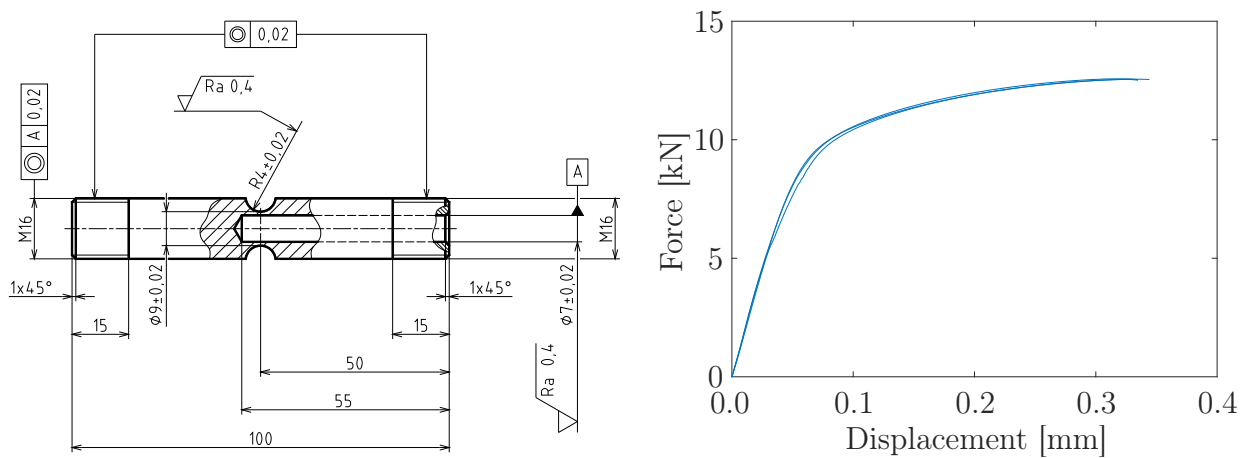


Figure 2.10: Drawing and responses of tensile notched tubular specimens [80]

## 2.6 Torsion of notched tubular specimen

Three torsional tests were realized using the notched tubular specimen (Fig. 2.11) under the rate of 0.001 rad/s. MTS 809 Axial/Torsional Testing System was employed and the angle of rotation was read from 646 Hydraulic Collet Grip. The wall thickness in the process zone was designed even thinner than the one in the case of tensile notched tubular specimen so that the crack initiation was followed by a rapid failure. The responses are displayed in Fig. 2.11 [80].

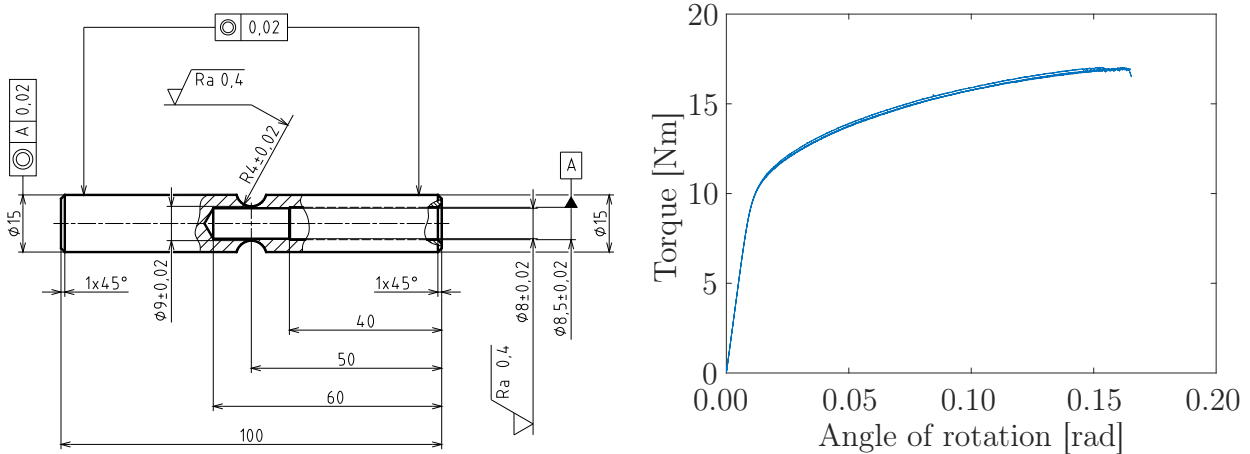


Figure 2.11: Drawing and responses of torsional notched tubular specimens [80]

## 3 Material modelling

The first feature of the material model is the elasticity – isotropic or anisotropic. Then, it is followed by the relationship of stress and plastic strain – the constitutive (hardening) law, which may be isotropic (defined by the flow curve), kinematic (describing the Bauschinger effect) or combined, prescribing the behaviour of yield surface defined by the yield criterion. The criterion may be isotropic or anisotropic, whereas quadratic or not, eventually stress triaxiality dependent. Finally, the flow rule – associated or not – defines the plastic strain increment direction. All parts of the model are described in the following sections.

All the computations were realized in Abaqus 2019. The mesh dependency was treated by using the same characteristic elements size of 0.075 mm within the gauge section in all numerical simulations. The mapped mesh was created as depicted in Fig. 3.1, where the smooth cylindrical specimen is omitted as the mesh layout is obvious, when  $3 \times 15$  mm rectangle was modelled. All the tests were modelled using the axial symmetry with CAX4R four-node bilinear quadrilateral elements with reduced integration and hourglass control, apart from the torsion and compression, which were modelled in three dimensions with C3D8R eight-node linear brick elements with reduced integration and hourglass control. The upper tubular part of torsional specimen, which did not undergo any deformation, was meshed with elements having a size of 0.2 mm. So as the parts of the cylinder, modelled with respecting the vertical and horizontal planes of symmetry, in a distance of 1.5 mm from the notch. Moreover, R3D4 four-node bilinear quadrilateral rigid elements with the size of 0.2 mm were utilized for the tool in the upsetting test, where the friction coefficient of 0.05 was applied (the punch is not displayed in Fig. 3.1). It was identified on the basis of deformations – barrelling and stick and slip regions. The simulation time was 0.1 s and the mass scaling with time increment of  $1 \times 10^{-7}$  s was employed for torsion and compression in order to speed up the computations, while the kinetic energy was checked in order to be negligible when compared to the total energy.

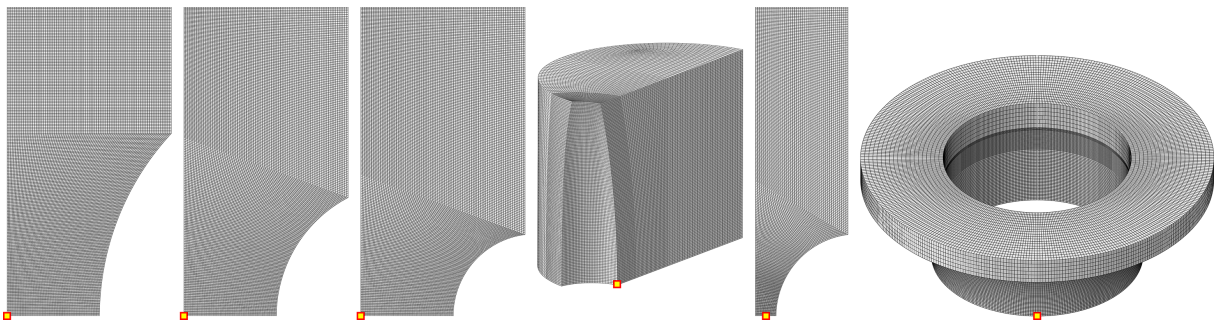


Figure 3.1: Meshed specimens with highlighted crack initiation locations (not in scale)

### 3.1 Model of elasticity

The isotropic elastic model of material was adopted, as mentioned earlier. The material constants used for the computations are given in Table 3.1 together with physical property needed for the calculation within the explicit finite element method, which was utilized due to its conditional stability allowing the crack initiation and propagation by means of element deletion. In such a case, the implicit algorithm is not capable of solution convergence [80].

Table 3.1: Elastic constants and specific mass utilized within computations

Young's modulus [MPa]	Poisson's ratio [-]	Density [ $\text{kg} \cdot \text{m}^{-3}$ ]
72500	0.34	2770

### 3.2 Model of plasticity

The isotropic plastic behaviour was assumed, as discussed earlier. All the parts of the plasticity model are introduced in the following subsections.

#### 3.2.1 Constitutive law

All the following yield criteria will share the same hardening law at the axisymmetric tension. The flow curve was identified against the standard tensile test of smooth cylindrical specimen, as described in the Section 2.2. First, the engineering strains and stresses were recalculated into true quantities up to the ultimate tensile strength (Fig. 3.2). Beyond that, the curve was extrapolated and the trial and error method was employed until the satisfying match between the average experiment and computation was achieved [80].

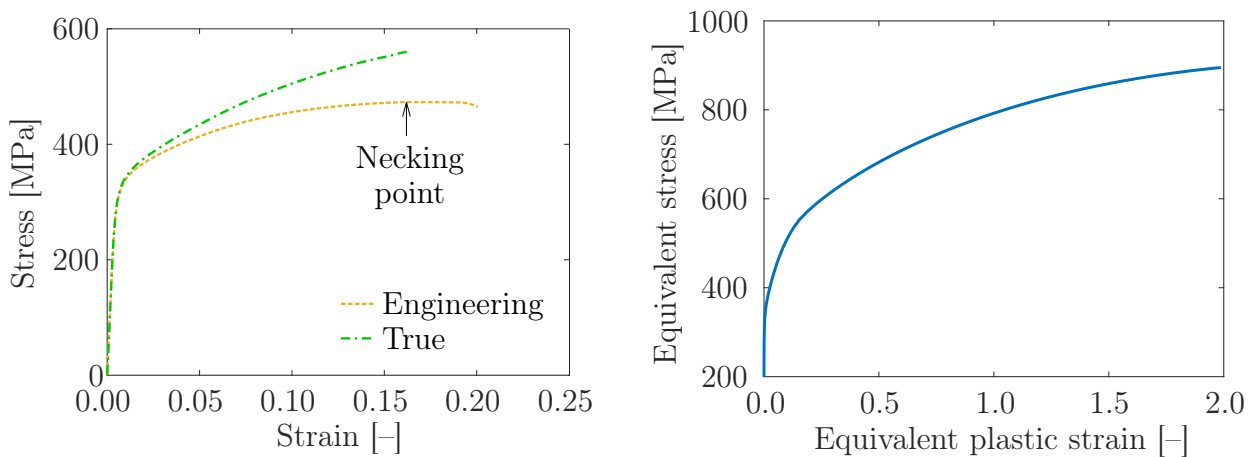


Figure 3.2: Stress–strain curves and calibrated conventional multi-linear flow curve [80]

Calibrated multi-linear flow curve is depicted in Fig. 3.2 and named as conventional. There is also a flow curve of matrix, which will be introduced due to the adopted plasticity damage approach later within this section [80].

### 3.2.2 Von Mises yield criterion with associated flow rule

The idea of quadratic yield criterion was first formulated by Maxwell in a letter to Kelvin. Huber [112] presented the principal on the basis of shear energy. Von Mises [113] proposed that yielding occurs when the second invariant of deviatoric stress tensor reaches a critical value. Finally, Hencky [114] interpreted it as a critical value of elastic energy of distortion.

The yield function can be written as

$$f = \bar{\sigma} - \sigma_y, \quad (3.1)$$

where  $\sigma_y$  is the yield stress and  $\bar{\sigma}$  is the equivalent stress defined as

$$\bar{\sigma} = \sqrt{\frac{3}{2} (\underline{s} : \underline{s})}. \quad (3.2)$$

The associated flow rule is given by

$$\frac{\partial f}{\partial \underline{\sigma}} = \frac{3}{2} \frac{\underline{s}}{\bar{\sigma}}. \quad (3.3)$$

It should be noted that the outward normal is not unit when the above formulation is adopted.

Finally, the increment of plastic multiplier is explicitly written as

$$\Delta\lambda = \frac{\sigma_{tr} - \sigma_y}{3G + H}, \quad (3.4)$$

where  $\sigma_{tr}$  is the trial stress,  $G$  is the shear modulus and  $H$  is the plastic modulus.

### 3.2.3 Kroon–Faleskog yield criterion with associated flow rule

Kroon and Faleskog [115] proposed a yield function (Kroon–Faleskog), which was dependent on the second and third invariants of deviatoric stress tensor. The yield function was

$$f = \bar{\sigma} - k\sigma_y, \quad (3.5)$$

where  $k$  is the yield correction function defined as

$$\begin{aligned} k &= 1 - \mu (1 - \xi^2) \left( \frac{1 + \xi_0^{\frac{1}{a}}}{[1 - \xi^2]^{\frac{1}{a}} + \xi_0^{\frac{1}{a}}} \right)^a \\ &= 1 - \mu \sin^2(3\theta_L) \left( \frac{1 + \xi_0^{\frac{1}{a}}}{\sin^{\frac{2}{a}}(3\theta_L) + \xi_0^{\frac{1}{a}}} \right)^a, \end{aligned} \quad (3.6)$$

where  $\mu$ ,  $\xi_0$  and  $a$  are the material constants.

The associated flow rule is given by the derivative of the yield function as

$$\frac{\partial f}{\partial \underline{\sigma}} = \frac{3}{2} \frac{\underline{s}}{\underline{\sigma}} - 3 \frac{dk}{d\xi} \left( 2 \frac{3}{2} \frac{\underline{s}}{\underline{\sigma}} \cdot \frac{3}{2} \frac{\underline{s}}{\underline{\sigma}} - \underline{I} - \xi \frac{3}{2} \frac{\underline{s}}{\underline{\sigma}} \right), \quad (3.7)$$

where  $\cdot$  is the dot product,  $\underline{I}$  is the identity matrix and the derivative is

$$\frac{dk}{d\xi} = \frac{2\mu \left(1 + \xi_0^{\frac{1}{a}}\right)^a \xi_0^{\frac{1}{a}} \xi}{\left([1 - \xi^2]^{\frac{1}{a}} + \xi_0^{\frac{1}{a}}\right)^{a+1}}. \quad (3.8)$$

Note that the first term in Eq. 3.7 is analogical to Eq. 3.3. Moreover, Kroon–Faleskog yield criterion is symmetric with respect to the generalized shear ( $\xi = 0$ ), which implies that the yield correction function is an even function, so  $k(\xi) = k(-\xi)$ . It simplifies into von Mises yield criterion when  $\mu = 0$  and roughly approaches Tresca yield criterion [116] when  $\mu = 1 - \sqrt{3}/2$ , yet with round corners unlike to Tresca yield criterion [116] exhibiting a singularity.

The plastic multiplier increment was calculated similarly to Eq. 3.4 according to the following expression

$$\Delta\lambda = \frac{\sigma_{tr} - k\sigma_y}{3G + kH}, \quad (3.9)$$

containing only the yield correction function additionally.

The yield criterion was implemented into Abaqus using the Vectorized User MATERIAL (VUMAT) subroutine. Then, it was calibrated by the trial and error method towards the experiments at generalized shear (tension and torsion of notched tube). Calibrated material constants are given in Table 3.2 with the yield locus depicted in Fig. 3.3 compared to the von Mises one, where  $\sigma_I$ ,  $\sigma_{II}$  and  $\sigma_{III}$  are the principal stresses not ordered according to the magnitude [80].

Table 3.2: Calibrated material constants for Kroon–Faleskog yield criterion [80]

$\mu$ [-]	$\xi_0$ [-]	$a$ [-]
0.123	0.180	4.000

The curvature was checked to ensure that the yield surface is convex according to the expression for polar coordinates in the form

$$\kappa = \frac{r^2 + 2 \left(\frac{dr}{d\theta_L}\right)^2 - r \frac{d^2r}{d\theta_L^2}}{\left(r^2 + \left(\frac{dr}{d\theta_L}\right)^2\right)^{\frac{3}{2}}} > 0, \quad (3.10)$$

where  $r$  is the radial coordinate of cylindrical coordinate system dependent on the Lode angle<sup>3</sup> through the yield correction function as

$$r = k \sqrt{\frac{2}{3}} \sigma_y. \quad (3.11)$$

<sup>3</sup> More details on coordinate systems are given in Appendix A.

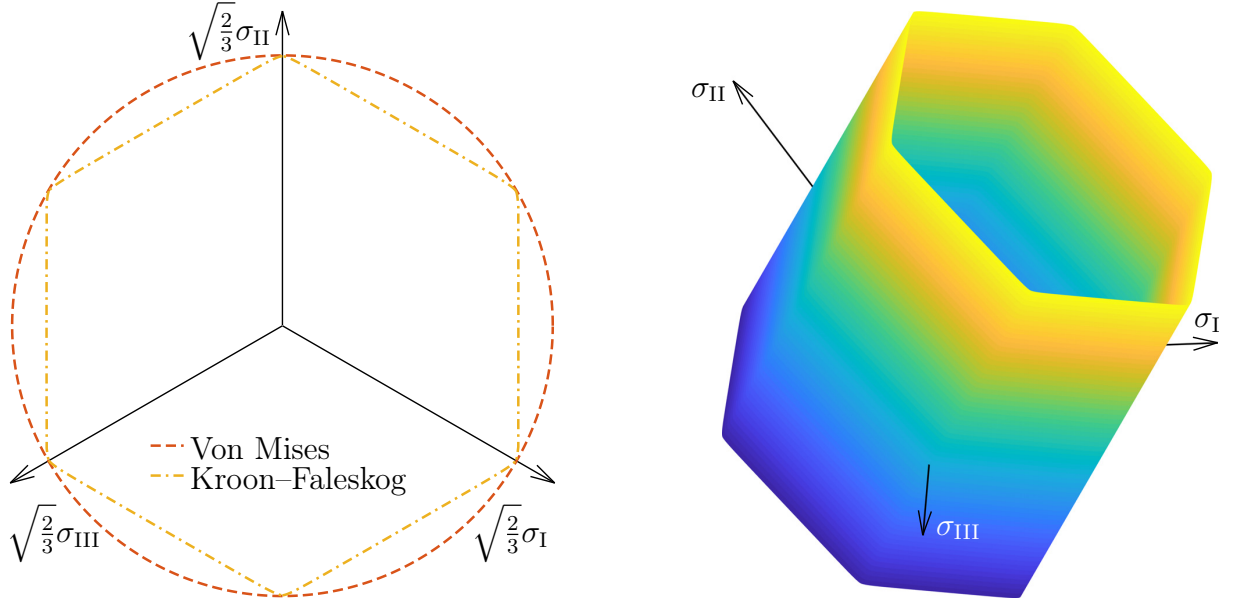


Figure 3.3: Calibrated Koon–Faleskog yield criterion compared to the von Mises one [80]

Then, the respective derivatives are

$$\frac{dr}{d\theta_L} = \frac{dk}{d\theta_L} \sqrt{\frac{2}{3}} \sigma_y = -3\mu \frac{\left(1 + \xi_0^{\frac{1}{a}}\right)^a \xi_0^{\frac{1}{a}}}{\left(\sin^{\frac{2}{a}}(3\theta_L) + \xi_0^{\frac{1}{a}}\right)^{a+1}} \sin(6\theta_L) \sqrt{\frac{2}{3}} \sigma_y, \quad (3.12)$$

$$\begin{aligned} \frac{d^2r}{d\theta_L^2} = \frac{d^2k}{d\theta_L^2} \sqrt{\frac{2}{3}} \sigma_y = 9\mu \frac{\left(1 + \xi_0^{\frac{1}{a}}\right)^a \xi_0^{\frac{1}{a}}}{\left(\sin^{\frac{2}{a}}(3\theta_L) + \xi_0^{\frac{1}{a}}\right)^{a+1}} \sqrt{\frac{2}{3}} \sigma_y \\ \times \left( \frac{a+1}{a} \frac{\sin^{\frac{2}{a}}(3\theta_L)}{\sin^{\frac{2}{a}}(3\theta_L) + \xi_0^{\frac{1}{a}}} 4 \cos^2(3\theta_L) - 4 \cos^2(3\theta_L) + 2 \right). \end{aligned} \quad (3.13)$$

The curvature was modified for easier plotting according to Koon and Faleskog [115] as

$$\bar{\kappa} = \frac{\ln\left(1 + \sqrt{\frac{2}{3}} \sigma_y \kappa\right)}{\ln(2)}. \quad (3.14)$$

The smoothness of the yield surface is ensured, when the curvature is finite, which was satisfied as well.

### 3.2.4 Bai–Wierzbicki yield criterion with deviatoric associated flow rule

Bai and Wierzbicki [43] (it was Bai [44] first actually) proposed a yield criterion dependent on the stress triaxiality and normalized third invariant of deviatoric stress tensor.

Due to the easier implementation, the yield correction function was introduced as in the case of Kroon–Faleskog yield criterion in Eq. 3.6 as

$$k = (1 - c_\eta [\eta - \eta_0]) \left( c_s + [c_a - c_s] \left[ \gamma - \frac{\gamma^{m+1}}{m+1} \right] \right), \quad (3.15)$$

where  $\eta_0$  is the initial stress triaxiality (serving as another material constant),  $c_\eta$ ,  $c_s$  and  $m$  are the material constants and  $\gamma$  is the function of deviatoric stress tensor as

$$\gamma = \frac{\sqrt{3}}{2 - \sqrt{3}} \left( \sec \left( \frac{1}{3} \arcsin[\xi] \right) - 1 \right) = \frac{\sqrt{3}}{2 - \sqrt{3}} \left( \sec \left( \frac{\pi}{6} - \theta_L \right) - 1 \right). \quad (3.16)$$

It should be noted that the secant is an even trigonometric function. Therefore, Bai and Wierzbicki [43] used  $\sec(\theta_L - \pi/6)$ . Finally,  $c_a$  is the function distinguishing between the tension and compression as

$$c_a = \begin{cases} c_t & \text{if } \xi \geq 0 \\ c_c & \text{if } \xi < 0 \end{cases}, \quad (3.17)$$

where  $c_t$  and  $c_c$  are the material constants. It should be noted that Vershinin [117] pointed out that it was mistakenly assumed that  $\bar{\sigma} = \sigma_y$ , which is not the case for the yield criteria dependent on the stress triaxiality and/or deviatoric stress tensor. Nevertheless, the deviatoric associated flow rule is given by Bai and Wierzbicki [43] by the chain rule as

$$\begin{aligned} \frac{\partial f}{\partial \underline{\sigma}} &= \frac{\partial \bar{\sigma}}{\partial \underline{\sigma}} + \sigma_y c_\eta \left( c_s + [c_a - c_s] \left[ \gamma - \frac{\gamma^{m+1}}{m+1} \right] \right) \frac{\partial \eta}{\partial \underline{\sigma}} \\ &\quad - \sigma_y (1 - c_\eta [\eta - \eta_0]) (c_a - c_s) (1 - \gamma^m) \frac{\partial \gamma}{\partial \underline{\sigma}}. \end{aligned} \quad (3.18)$$

The first derivative in Eq. 3.18 is analogical to Eq. 3.3 as

$$\frac{\partial \bar{\sigma}}{\partial \underline{\sigma}} = \frac{3}{2} \frac{\underline{s}}{\bar{\sigma}}. \quad (3.19)$$

The second derivative is

$$\frac{\partial \eta}{\partial \underline{\sigma}} = \frac{1}{3} \frac{I}{\bar{\sigma}} - \frac{3}{2} \frac{\underline{s}}{\bar{\sigma}^2} \eta. \quad (3.20)$$

Finally, the last derivative is

$$\frac{\partial \gamma}{\partial \underline{\sigma}} = \frac{3\sqrt{3}}{2 - \sqrt{3}} \frac{\tan \left( \frac{1}{3} \arcsin[\xi] \right)}{\cos \left( \frac{1}{3} \arcsin[\xi] \right)} \frac{1}{\bar{\sigma} \sqrt{1 - \xi^2}} \left( \frac{3}{2} \frac{\underline{s} \cdot \underline{s}}{\bar{\sigma}^2} - \frac{I}{3} - \frac{\xi \underline{s}}{2\bar{\sigma}} \right). \quad (3.21)$$

It should be noted that the outward normal is perpendicular to the yield surface only on the deviatoric (octahedral) plane<sup>4</sup> when the first term is eliminated from Eq. 3.20, therefore the deviatoric associativity of the flow rule.

The yield criterion simplifies into the von Mises one when either  $c_\eta = 0$  and  $c_c = c_s = c_t = 1$  or  $m = 0$ . It becomes the yield criterion proposed by Drucker and Prager [118] when  $c_\eta \neq 0$  while either  $c_c = c_s = c_t = 1$  or  $m = 0$ . Finally, it closely approaches the Tresca [116] yield criterion when  $c_\eta = 0$ ,  $c_s = \sqrt{3}/2$ ,  $c_c = c_t = 1$  and  $m \rightarrow \infty$ .

<sup>4</sup> More information on planes is given in Appendix A.

The plastic multiplier was calculated according to the same equation, as in the case of previous yield criterion (Eq. 3.9). The yield criterion was implemented into Abaqus using the VUMAT as in the previous case. Then, it was calibrated by the trial and error method towards all experiments. Calibrated material constants are in Table 3.3, while the yield locus is depicted in Fig. 3.4 [51].

Table 3.3: Calibrated material constants for Bai–Wierzbicki yield criterion [51]

$\eta_0$ [-]	$c_\eta$ [-]	$c_c$ [-]	$c_s$ [-]	$c_t$ [-]	$m$ [-]
0.20	0.09	1.01	0.88	1.00	20.0

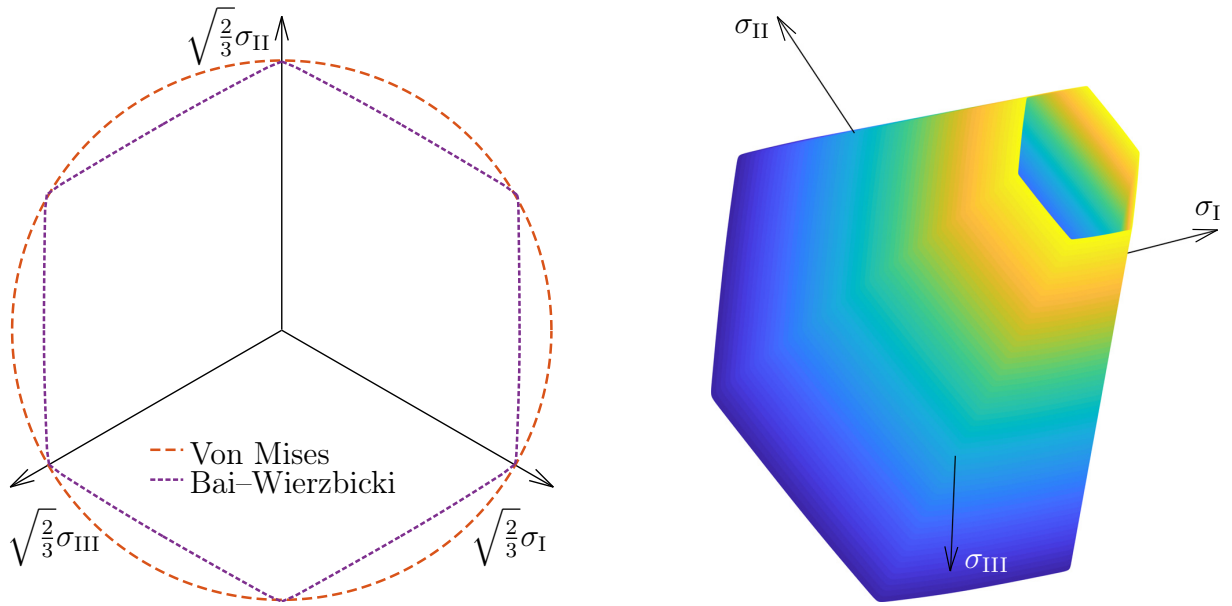


Figure 3.4: Calibrated Bai–Wierzbicki yield criterion compared to the von Mises one [51]

The yield surface convexity is dependent on the material constants  $c_c$ ,  $c_s$ ,  $c_t$  and  $m$ . Lian et al. [119] derived a simple criterion for the convexity,  $\sqrt{3}/2 \leq c_s/c_a \leq 1$ , which is independent on material constant  $m$ , which should be a positive integer. For full control, the curvature was calculated and checked again according to Eqs. 3.10 and 3.11. The first derivative is

$$\begin{aligned}
 \frac{dr}{d\theta_L} &= \frac{dk}{d\theta_L} \sqrt{\frac{2}{3}} \sigma_y \\
 &= (-1 + c_\eta [\eta - \eta_0]) (c_a - c_s) \frac{\sin(\frac{\pi}{6} - \theta_L)}{(\sqrt{3} - 2)^2 \cos^2(\frac{\pi}{6} - \theta_L)} \sqrt{\frac{2}{3}} \sigma_y \\
 &\quad \times \left( 2\sqrt{3} - 3 + \left( 3^{\frac{m}{2}+1} - 2 \times 3^{\frac{m}{2}+\frac{1}{2}} \right) \left[ \frac{-1 + \cos(\frac{\pi}{6} - \theta_L)}{(\sqrt{3} - 2) \cos(\frac{\pi}{6} - \theta_L)} \right]^m \right). \quad (3.22)
 \end{aligned}$$

The second derivative is

$$\begin{aligned}
\frac{d^2 r}{d\theta_L^2} &= \frac{d^2 k}{d\theta_L^2} \sqrt{\frac{2}{3}} \sigma_y \\
&= \frac{(1 - c_\eta [\eta - \eta_0]) (c_a - c_s)}{(\sqrt{3} - 2)^2 \cos^3 \left( \frac{\pi}{6} - \theta_L \right)} \\
&\quad \times \left( \left[ \left( 3^{\frac{m}{2}+1} - 2 \times 3^{\frac{m}{2}+\frac{1}{2}} \right) \left[ m - \cos \left( \frac{\pi}{6} - \theta_L \right) \right] \cos \left( \frac{\pi}{6} - \theta_L \right) \right. \right. \\
&\quad \left. \left. + (-2m - 4) 3^{\frac{m}{2}+\frac{1}{2}} + m 3^{\frac{m}{2}+1} + 6 \times 3^{\frac{m}{2}} \right] \left[ \frac{-1 + \cos \left( \frac{\pi}{6} - \theta_L \right)}{(\sqrt{3} - 2) \cos \left( \frac{\pi}{6} - \theta_L \right)} \right]^m \right. \\
&\quad \left. - 2 \left( \sqrt{3} - \frac{3}{2} \right) \left[ \cos^2 \left( \frac{\pi}{6} - \theta_L \right) - 2 \right] \right) \sqrt{\frac{2}{3}} \sigma_y. \tag{3.23}
\end{aligned}$$

The requirement on the finite curvature was satisfied, so the yield surface is smooth.

### 3.2.5 Comparison of calibrated yield criteria

The modified curvatures of all calibrated yield criteria are compared in Fig. 3.5.

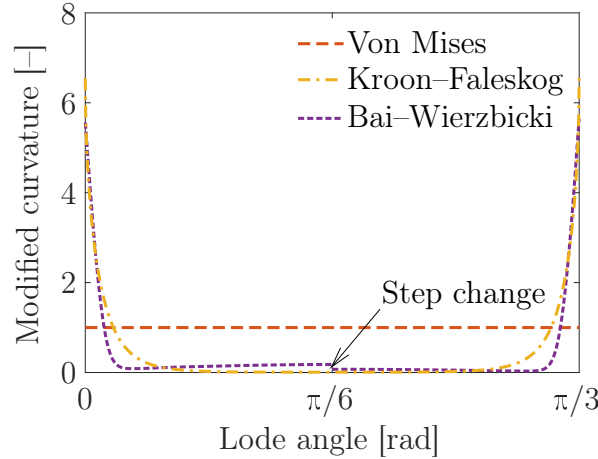


Figure 3.5: Modified curvatures of calibrated yield criteria

All the computations have been conducted with the use of conventional flow curve (Fig. 3.2) so far. Responses from all the standard tensile tests are depicted in Fig. 3.6. As anticipated, all the predicted force responses were almost identical for standard tensile test (Fig. 3.6), which was utilized for estimating the conventional flow curve. Only the Bai–Wierzbicki yield criterion with deviatoric associated flow rule produced slightly lower responses, even though  $c_t = 1.00$  (Table 3.3). Nevertheless, the deterioration is negligible in overall, because the yield criterion improved the remaining tensile tests of notched cylindrical specimens (Fig. 3.7) and it had globally the lowest error (Table 3.4). It was 16% compared to 21% for Kroon–Faleskog and 43% for von Mises yield criteria with associated flow rules. Therefore, the Bai–Wierzbicki yield criterion with deviatoric associated flow rule, which is the most complex one, will be utilized within further computations [51].

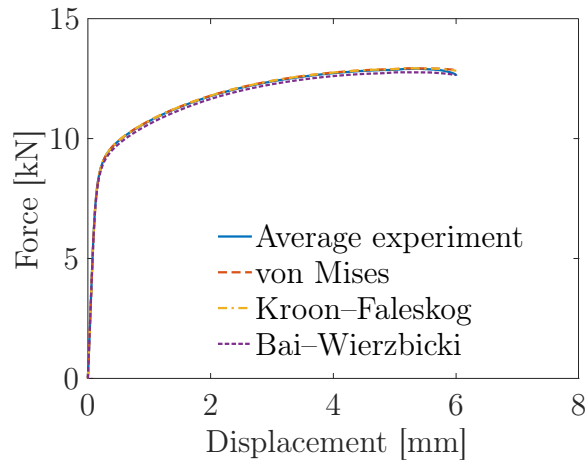


Figure 3.6: Responses for standard tension and all plasticity models considered [51]

All errors are summarized in Table 3.4 [51].

Table 3.4: Deviations between the experiments and all plasticity models considered [51]

Specimen	Von Mises	Kroon-Faleskog	Bai-Wierzbicki
Tensile smooth cylindrical [%]	0	0	1
Notched cylindrical with R13 [%]	3	3	2
Notched cylindrical with R6.5 [%]	7	6	4
Notched cylindrical with R4 [%]	4	3	1
Upsetting notched cylindrical [%]	2	4	2
Tensile notched tubular [%]	15	3	4
Torsional notched tubular [%]	12	2	2
Sum [%]	43	21	16

All the remaining responses are depicted in Fig. 3.7 [51].

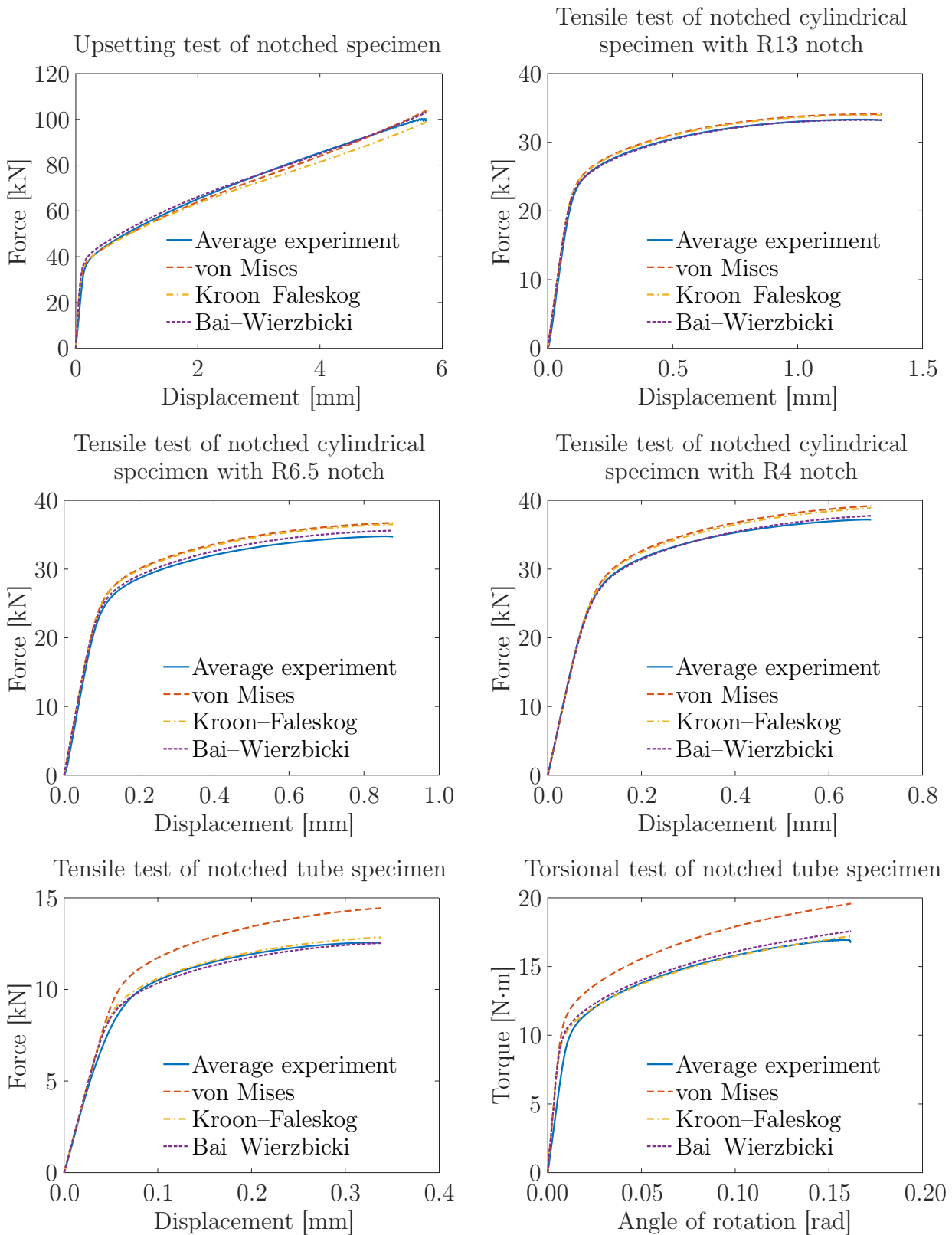


Figure 3.7: Responses for experiments and computations, except for the standard tension

The errors were computed according to

$$100 \sum \frac{|F_e - F_c|}{F_e}, \quad (3.24)$$

where  $F_e$  and  $F_c$  are the forces from experiment and computation, respectively, while all the responses were sampled with 200 points [51].

### 3.3 Model of damage

The non-linear damage accumulation is one of the key features to the possible solution of the problems with the non-proportional loading, although there have been some doubts [102] or other modelling approaches [120]. Lemaitre and Dufailly [121] described eight different methods of measuring the damage by the destructive as well as non-destructive methods covering the fractography and variation of the following quantities: density, ultrasonic wave propagation, cyclic plasticity response, tertiary creep response, microhardness, electrical potential and finally, the variation of Young's modulus, which is employed within the present thesis. Other method of investigating the damage evolution lies in the non-proportional tests, usually conducted on the notched tubular or cylindrical specimens under biaxial loading (tension–torsion), and following numerical analysis [97, 122]. The problem is that the damage accumulates in one material point when the specimen is pulled, but once the specimen is twisted, the damage accumulation continues in a different location, which was not critical in the first stage of loading during the tension. Theoretically, better results could be obtained by the two-step tests [123, 124, 125], which consist of pulling the specimen of one geometry until the fracture and then the same until a prescribed deformation. Once the test is interrupted at this deformation, the specimen is machined into a new geometry resulting in a different stress state, and pulled until the fracture. Cortese et al. [126] incorporated the fracture strain into the damage accumulation power law, which is micromechanically questionable as a completely different damage accumulation behaviour may occur in very close locations. The exponent may be greater than one in one location and lower than one in the other (for notched cylindrical specimen for example), therefore the damage accumulation would be decelerating in one location while rapidly accelerating in the other, which could be quite close to each other. Nevertheless, the most promising seems to be the biaxial loading of cruciform specimen [127, 128, 129]. When carefully prepared, there is no problem with migrating critical location or with the machining between the two steps, which may introduce undesirable effects.

The degradation of Young's modulus gives

$$D = \frac{\tilde{E}}{E}, \quad (3.25)$$

where  $\tilde{E}$  is the actual (degraded) modulus of elasticity. Three semi-cyclic, or loading–unloading, tests were conducted on the standard cylindrical specimen (Fig. 2.7). The specimen was unloaded after each 2% increment of engineering strain and then loaded again with the rate of 1 mm/min on Zwick Z250 Allround-Line, tCII, with Zwick multiXtens extensometer having the gauge length of 30 mm. Resulting Young's modulus degradation with fitted damage accumulation law is plotted in Fig. 3.8.

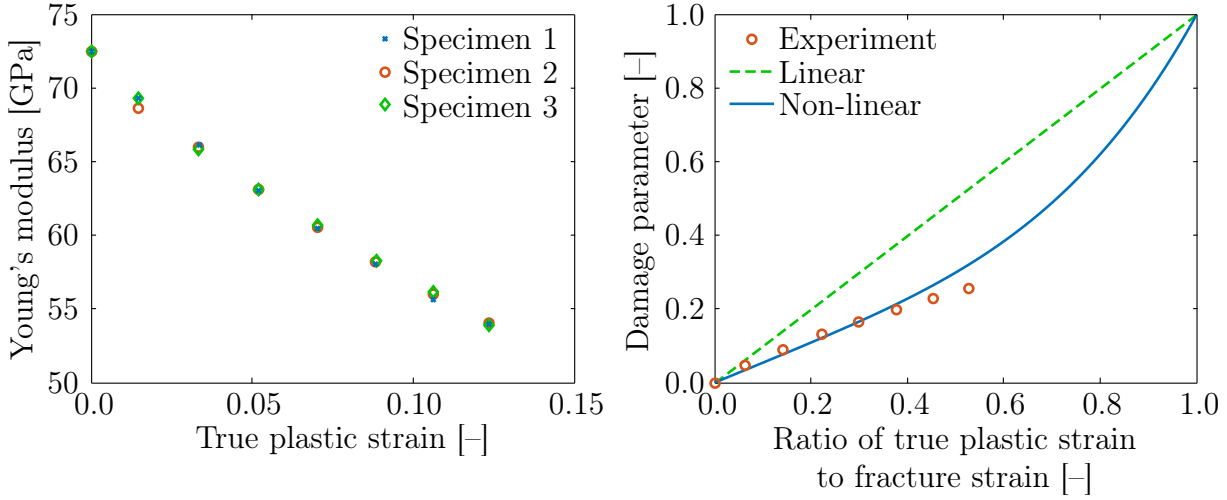


Figure 3.8: Damage evolution and fitted non-linear law [132]

The damage accumulation law was proposed according to the trend of experimental data, based on the double damage curve proposed by Manson and Halford [130] within the low-cycle fatigue, which was actually first published in [131]. After simplifying and adapting to the ductile fracture, the equation reads [80]

$$D = q_1 \int_0^{\bar{\varepsilon}_D} \frac{d\bar{\varepsilon}_p}{C_m + \bar{\varepsilon}_f} + q_2 (1 - q_1) \int_0^{\bar{\varepsilon}_D} \left( \frac{\bar{\varepsilon}_p}{C_m + \bar{\varepsilon}_f} \right)^{q_2-1} \frac{d\bar{\varepsilon}_p}{C_m + \bar{\varepsilon}_f}, \quad (3.26)$$

where  $q_1$  and  $q_2$  are the material constants, while  $q_2 > 0$  has to be always satisfied, and  $C_m$  is the additional material constant relating the micro and macro perspective of the damage indication. The non-linear law degenerates into linear, when either  $q_1 = 1$  or  $q_2 = 1$  and it becomes polynomial as the law proposed by Xue [79] when  $q_1 = 0$ . The damage accumulation rate may be decelerating, when either  $0 < q_1 < 1$  and  $0 < q_2 < 1$  or  $q_1 > 1$  and  $q_2 > 1$ , or accelerating, when  $0 < q_1 < 1$  and  $q_2 > 1$  or  $q_1 > 1$  and  $0 < q_2 < 1$ .

The material constants  $q_1$  and  $q_2$  were calibrated towards the experiments available until the ultimate tensile strength (Fig. 3.8) [132]. Beyond that point, the deformation was not uniform and therefore not directly readable in the location of damage accumulation (necking section).

All the simulations have been done with the conventional flow curve (Fig. 3.2) up to this point. From now on, the multi-linear flow curve of matrix was deployed in the following form [132]

$$\bar{\sigma} = (1 + \bar{\varepsilon}_p) \sigma_y, \quad (3.27)$$

so that finally, the yield function was used in the following form

$$f = \bar{\sigma} - w\tilde{\sigma} = \bar{\sigma} - w(1 + \bar{\varepsilon}_p)k\sigma_y = \bar{\sigma} - (1 - D^\beta)(1 + \bar{\varepsilon}_p)k\sigma_y. \quad (3.28)$$

The rest of the material constants,  $C_m$  and  $\beta$ , were calibrated against the standard tensile test as depicted in Fig. 3.9, where  $\hat{\varepsilon}_f$  is the fracture strain for a particular test [132].

All the damage-related material constants are given in Table 3.5. It should be noted that the loss of ellipticity and subsequent localization of field variables were not addressed.

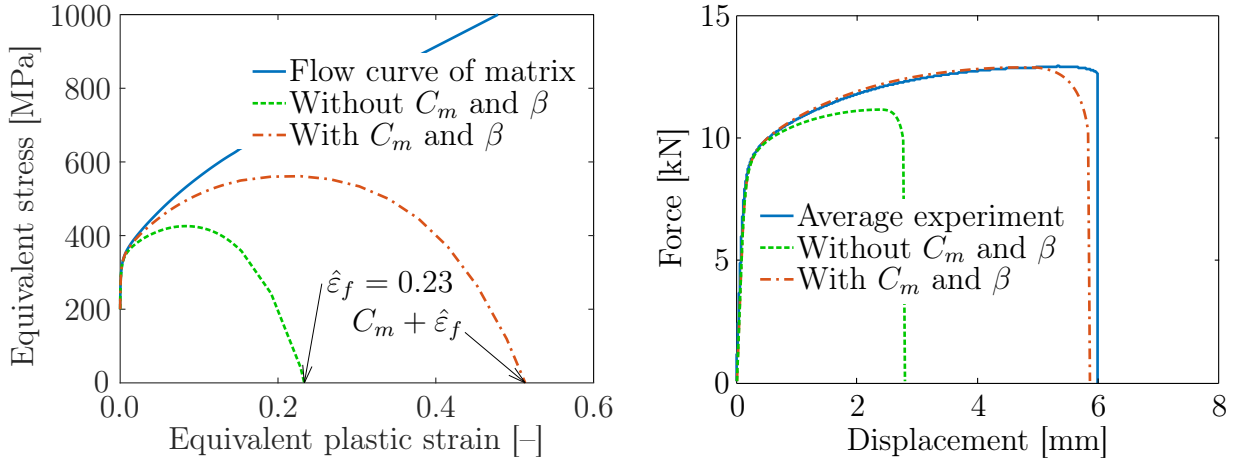


Figure 3.9: Flow curve of matrix with resulting force responses [132]

Table 3.5: Calibrated damage-related material constants [132]

$q_1$ [-]	$q_2$ [-]	$C_m$ [-]	$\beta$ [-]
0.54	4.00	0.28	1.10

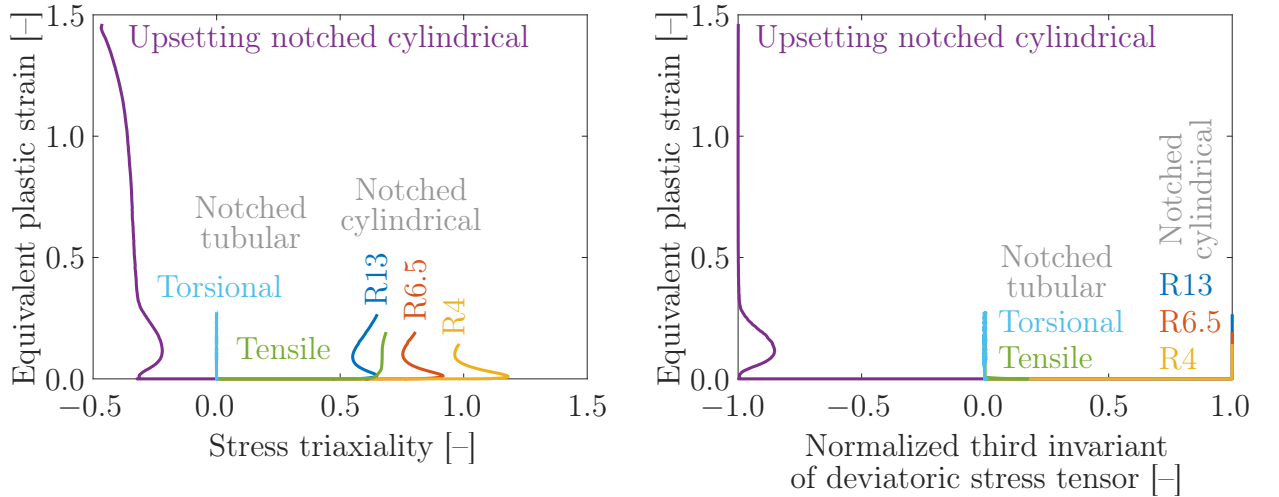


Figure 3.10: Evolutions of stress triaxiality and normalized third invariant of deviatoric stress tensor before the averaging

Finally, the points for ductile fracture criteria calibration were obtained through the integration respecting the non-linear damage accumulation as [132]

$$\eta_a = q_1 \int_0^{\hat{\epsilon}_f} \eta \frac{d\bar{\epsilon}_p}{\hat{\epsilon}_f} + q_2 (1 - q_1) \int_0^{\hat{\epsilon}_f} \eta \left( \frac{\bar{\epsilon}_p}{\hat{\epsilon}_f} \right)^{q_2-1} \frac{d\bar{\epsilon}_p}{\hat{\epsilon}_f}, \quad (3.29)$$

$$\xi_a = q_1 \int_0^{\hat{\epsilon}_f} \xi \frac{d\bar{\epsilon}_p}{\hat{\epsilon}_f} + q_2 (1 - q_1) \int_0^{\hat{\epsilon}_f} \xi \left( \frac{\bar{\epsilon}_p}{\hat{\epsilon}_f} \right)^{q_2-1} \frac{d\bar{\epsilon}_p}{\hat{\epsilon}_f}, \quad (3.30)$$

where  $\xi_a$  is the average normalized third invariant of deviatoric stress tensor.

The averaging was realized utilizing the trapezoidal numerical integration within MATLAB R2019a with all the results summarized in Table 3.6. The evolutions of the stress triaxiality and normalized third invariant of deviatoric stress tensor (Fig. 3.10) were extracted for the integration from the crack initiation locations, which are highlighted in Fig. 3.1, from the simulations depicted in Fig. 3.7 (carried out with the conventional flow curve).

Table 3.6: Points used for the ductile fracture criteria calibration

Specimen	Fracture strain [-]	Average stress triaxiality [-]	Average normalized third invariant of deviatoric stress tensor [-]
Notched cylindrical with R13	0.266	0.606	1.000
Notched cylindrical with R6.5	0.193	0.790	1.000
Notched cylindrical with R4	0.144	1.001	1.000
Upsetting notched cylindrical	1.463	-0.369	-0.991
Tensile notched tubular	0.193	0.672	0.001
Torsional notched tubular	0.274	-0.001	-0.002

### 3.4 Model of failure

Three ductile fracture criteria were selected so that a broad range of possibilities is examined and then calibrated towards the points from Table 3.6. The first was extended Mohr–Coulomb criterion proposed along the Bai–Wierzbicki yield criterion, then the model proposed on a different basis by Lou et al. [53], and finally the KHPS2 criterion developed by the author with his colleagues. The whole calibration was realized within MATLAB R2019a. The minimum of constrained non-linear multi-variable target function was found using the created optimization problem structure that included the initial guess of material constants and their lower and upper bounds where appropriate.

### 3.4.1 Extended Mohr–Coulomb criterion

The following polynomial law inspired by the Hollomon one [46] may be adopted as

$$\bar{\sigma}_f = kK\bar{\varepsilon}_f^n, \quad (3.31)$$

where  $\bar{\sigma}_f$  is the fracture stress.

Then, the extended Mohr–Coulomb criterion will be called the one proposed by Bai and Wierzbicki [45] and slightly modified by Kubík et al. [51] as

$$\begin{aligned} \bar{\varepsilon}_f = & \left[ \frac{K}{M_2} k \left( \sqrt{\frac{1+M_1^2}{3}} \cos\left(\frac{1}{3} \arcsin[\xi]\right) \right. \right. \\ & \left. \left. + M_1 \left[ \eta + \frac{1}{3} \sin\left(\frac{1}{3} \arcsin[\xi]\right) \right] \right) \right]^{-\frac{1}{n}}, \end{aligned} \quad (3.32)$$

where  $M_1$  and  $M_2$  are the material constants. It is slightly different from what was proposed by Bai and Wierzbicki [45] (Eq. 1.15), because it uses the yield correction function exactly without any simplifications. Moreover, Eq. 3.32 is not formally correct as the stress–strain relationship is used in the multi-linear form with respect to Eq. 3.27 and not in the Hollomon [46] inspired power law-based form (Eq. 3.31). Finally, the cut-off stress triaxiality is

$$\eta_c = -\frac{1}{M_1} \sqrt{\frac{1+M_1^2}{3}} \cos\left(\frac{1}{3} \arcsin[\xi]\right) - \frac{1}{3} \sin\left(\frac{1}{3} \arcsin[\xi]\right). \quad (3.33)$$

The first constraint  $\eta_c - \eta_a < 0$  ensures that there is no negative fracture strain, which is physically unreal, and common to all criteria utilized within this thesis. The second constraint  $M_1 > 0$  makes sure that the cut-off plane will be convex. The strength coefficient may be even omitted (set equal to one) and the strain hardening exponent considered as another material constant for calibration along with  $M_1$  and  $M_2$ , which gives more flexibility to the criterion [132, 133]. Nevertheless, such an approach was not pursued within the present thesis. It should be noted that it does not seem to be of such an importance, when two material constants remain to be calibrated.

Eq. 3.31 was fitted to the conventional flow curve (Fig. 3.11) as all the simulations for calibration were done using that constitutive law, while the fracture stress was considered to be an equivalent stress, the yield correction function equal to one and the fracture strain be an equivalent plastic strain. Calibrated material constants are altogether given in Table 3.7. It may be pointed out that even the simplest polynomial law is often capable of a good fit. Therefore, more complicated formulas (Fig. 2.1) are not necessary.

Table 3.7: Calibrated material constants for the extended Mohr–Coulomb criterion

$K$ [MPa]	$n$ [-]	$M_1$ [-]	$M_2$ [MPa]
789.1	0.190	0.187	334.2

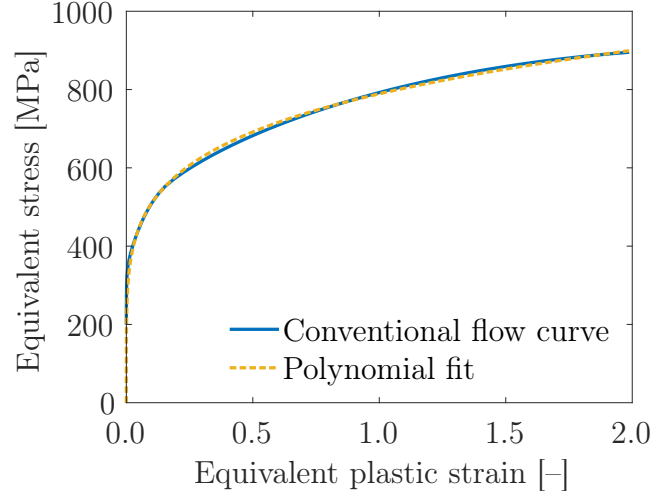


Figure 3.11: Polynomial constitutive law fitted to the conventional flow curve

### 3.4.2 Lou–Huh criterion

Lou–Huh criterion will be called the one proposed by Lou et al. [53] in the form that reads

$$\bar{\varepsilon}_f = K_3 \left( \frac{2}{\sqrt{3} [1 + \tan^2 (-\frac{1}{3} \arcsin[\xi])]} \right)^{-K_1} \times \left\langle \frac{3}{1 + 2K_4 + 3K_5} \left( \eta + K_4 \frac{\sqrt{3} - \tan (-\frac{1}{3} \arcsin[\xi])}{3\sqrt{1 + \tan^2 (-\frac{1}{3} \arcsin[\xi])}} + K_5 \right) \right\rangle^{-K_2}, \quad (3.34)$$

where  $K_1, \dots, K_5$  are the material constants with a condition that

$$K_4 \neq -\frac{1}{2} - \frac{3}{2}K_5. \quad (3.35)$$

Furthermore, the cut-off stress triaxiality is

$$\eta_c = -K_4 \frac{\sqrt{3} - \tan (-\frac{1}{3} \arcsin[\xi])}{3\sqrt{1 + \tan^2 (-\frac{1}{3} \arcsin[\xi])}} - K_5. \quad (3.36)$$

Correct calibration is enforced by the constraint  $\eta_c - \eta_a < 0$  and the convexity of cut-off plane, discussed further, is reached by the condition  $K_4 > 0$ .

The constraint  $\eta_c = -0.5$  at  $\xi = -1$  was posed in order to obtain the cut-off in a reasonable range as the criterion is too flexible without that condition. It is a similar approach to the one presented by Lou et al. [53] or Lou and Yoon [54]. Finally, all the material constants are presented in Table 3.8.

Table 3.8: Calibrated material constants for the Lou–Huh criterion

$K_1$ [-]	$K_2$ [-]	$K_3$ [-]	$K_4$ [-]	$K_5$ [-]
1.965	0.855	0.261	1.579	-0.026

### 3.4.3 KHPS2 criterion

KHPS2 criterion proposed by Šebek et al. [132], which was actually first published by Hůlka [134], follows the KHPS criterion proposed by Kubík et al. [135]. It has a hyperbolic shape while the foci of rectangular hyperbolas obey quadratic dependency on the normalized third invariant of deviatoric stress tensor. The fracture strain reads

$$\begin{aligned} \bar{\varepsilon}_f = & \left[ \frac{1}{2} \left( \frac{G_4}{\langle \eta - \eta_c \rangle} + \frac{G_5}{\langle \eta - \eta_c \rangle} \right) - \frac{G_6}{\langle \eta - \eta_c \rangle} \right] \xi^2 \\ & + \frac{1}{2} \left( \frac{G_4}{\langle \eta - \eta_c \rangle} - \frac{G_5}{\langle \eta - \eta_c \rangle} \right) \xi + \frac{G_6}{\langle \eta - \eta_c \rangle}, \end{aligned} \quad (3.37)$$

where  $G_1, \dots, G_6$  are the material constants. The parabolic cut-off stress triaxiality is

$$\eta_c = - \left( G_3 + \frac{G_1 - G_3}{2} - G_2 \right) \xi^2 - \frac{G_1 - G_3}{2} \xi - G_2. \quad (3.38)$$

The first three material constants,  $G_1, \dots, G_3$ , are the additive inverses of cut-off plane distance in the stress triaxiality, as illustrated in Fig. 3.12. The last three material constants have to be positive,  $G_4, \dots, G_6 > 0$ , because those influence the vertices of rectangular hyperbolas (Fig. 3.12). In order to properly calibrate the criterion, the constraint  $\eta_c - \eta_a < 0$  has to be satisfied along the convexity of the cut-off stress triaxiality required by the condition posed on the signed curvature in the Cartesian coordinates as

$$\kappa = \frac{\frac{d^2 \eta_c}{d\xi^2}}{\left( 1 + \left( \frac{d\eta_c}{d\xi} \right)^2 \right)^{\frac{3}{2}}} = \frac{-(G_1 - 2G_2 + G_3)}{\left( 1 + ([G_1 - 2G_2 + G_3] \xi + \frac{G_1 - G_3}{2})^2 \right)^{\frac{3}{2}}} > 0. \quad (3.39)$$

This can be solved more easily using the second derivative of a function. Therefore, the cut-off is convex if

$$\frac{d^2 \eta_c}{d\xi^2} = -(G_1 - 2G_2 + G_3) > 0, \quad (3.40)$$

which is consistent with Eq. 3.39. It was discussed earlier that this cut-off shape is more natural when expecting lower ductility for generalized shear ( $\xi = 0$ ) than for the axisymmetric tension or compression. Nevertheless, this is on the contrary as it is utilized sometimes [7, 53, 54, 136].

All the calibrated material constants are summarized in Table 3.9.



Table 3.10: Deviations of points used for calibration from the calibrated fracture criteria

Specimen	Extended Mohr–Coulomb	Lou–Huh	KHPS2
Notched cylindrical with R13 [%]	11	16	1.8
Notched cylindrical with R6.5 [%]	2.0	5.5	0.2
Notched cylindrical with R4 [%]	12	28	0.7
Upsetting notched cylindrical [%]	0.2	0.2	0.4
Tensile notched tubular [%]	18	9.1	2.3
Torsional notched tubular [%]	16	3.5	1.0
Sum [%]	59	62	6.5

The states of plane stress and cut-off stress triaxialities are compared in Fig. 3.13, where  $\sigma_2$  and  $\sigma_3$  are the second (middle) and the third (minimum) principal stresses. The regions of plane stress with corresponding zero principal stresses are highlighted in Fig. 3.13 too. In Figs. 3.13 and 3.14, the blue square represents the upsetting notched cylindrical specimen, the magenta hexagram represents the tensile notched tubular specimen, the magenta diamond represents the torsional notched tubular specimen and the red circles represent the notched cylindrical specimens.

All the calibrated ductile fracture criteria with respective points for calibration that were described earlier are depicted in Fig. 3.14. It can be seen that both the extended Mohr–Coulomb and Lou–Huh criteria have more flat cut-off planes than KHPS2 criterion. Moreover, the extended Mohr–Coulomb criterion has the cut-off plane further in the negative stress triaxiality.

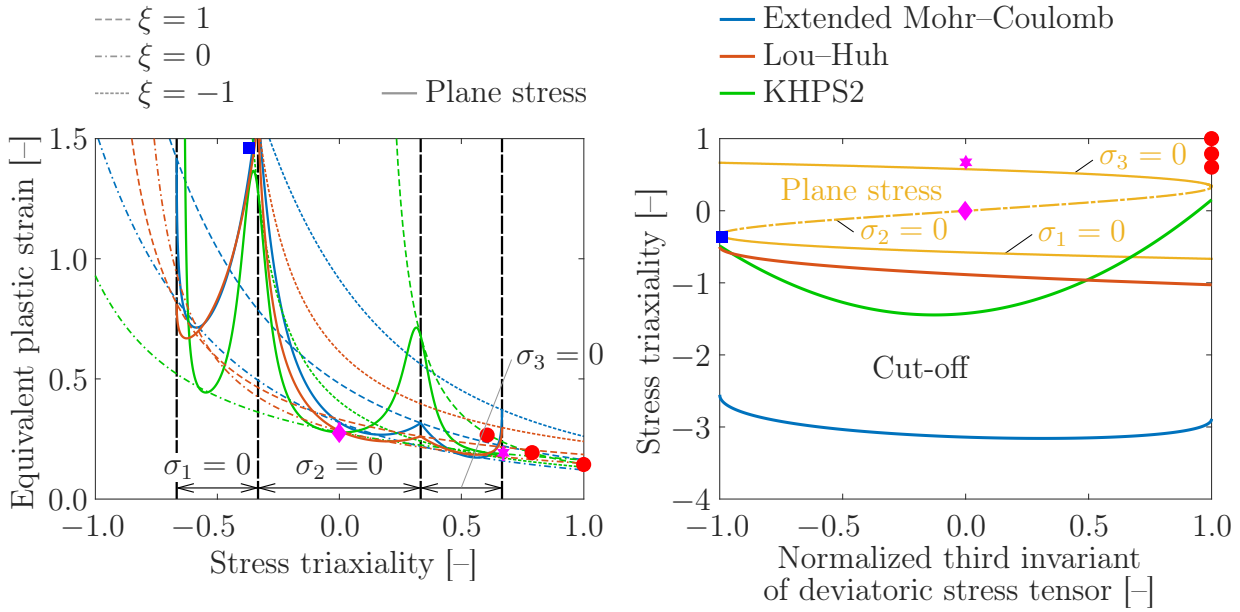


Figure 3.13: Comparison of states of plane stress and cut-off stress triaxialities

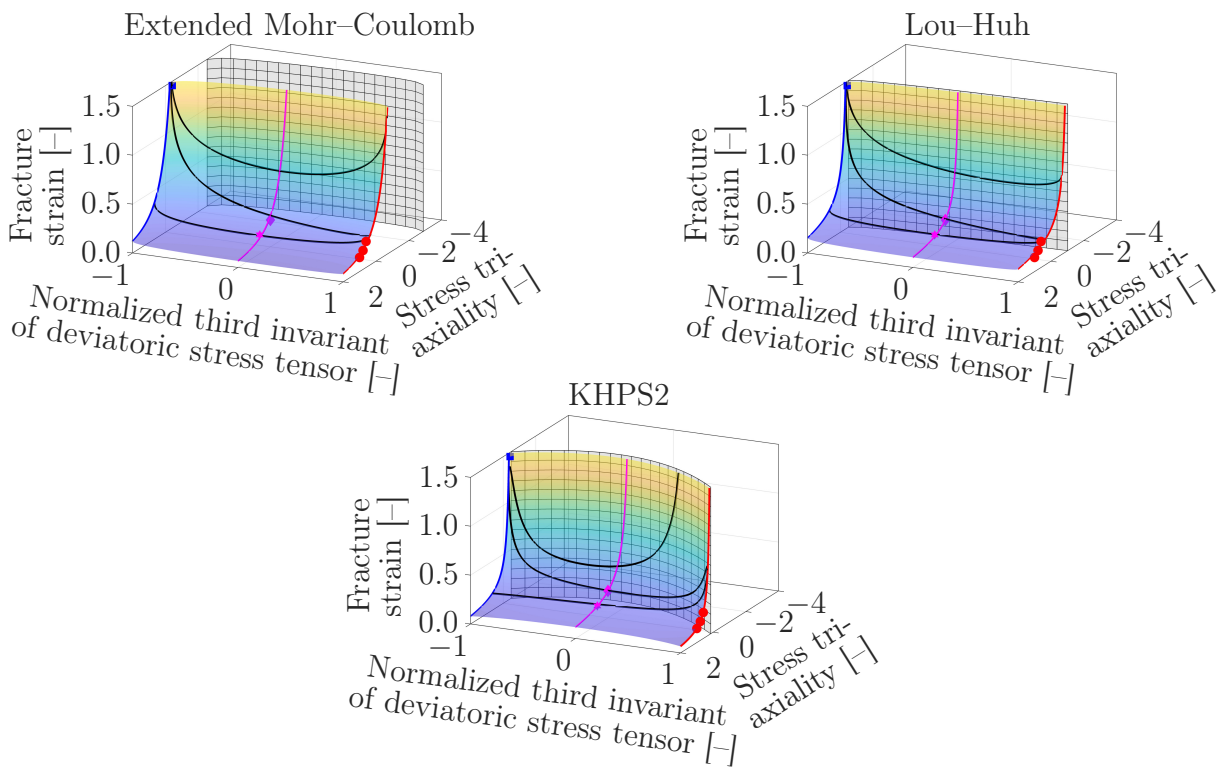


Figure 3.14: Calibrated ductile fracture criteria with the points used for fitting

## 4 Application

The above developed material model is applied to the small punch testing and three-point bending in order to reveal the predictability. These two experiments were not included in the calibration procedure. The quantitative as well as qualitative assessment was conducted.

### 4.1 Small punch testing

Three small punch tests were conducted using the Zwick Z250 Allround-Line, tCII, with the Zwick multiXtens extensometer and loading rate of 1 mm/min. The detailed drawing of the apparatus with specimen is given in Fig. 4.1 as the test has not been standardized yet. The responses are given in Fig. 4.1 [101], even though the experiments were first published by Šebek et al. [137].

The cylindrical rod with a diameter of  $8 \pm 0.02$  mm was machined with surface roughness of  $0.4 \mu\text{m}$ . The pieces of  $0.6 \pm 0.02$  mm thickness were cut by the electrical discharge machining. Then, the grinding using the sandpapers with P600, P1200 and P2000 roughness was applied. Finally, the polishing with 3 and  $1 \mu\text{m}$  grain-sized diamond paste was utilized until the required thickness of  $0.5 \pm 0.005$  mm was achieved [101].

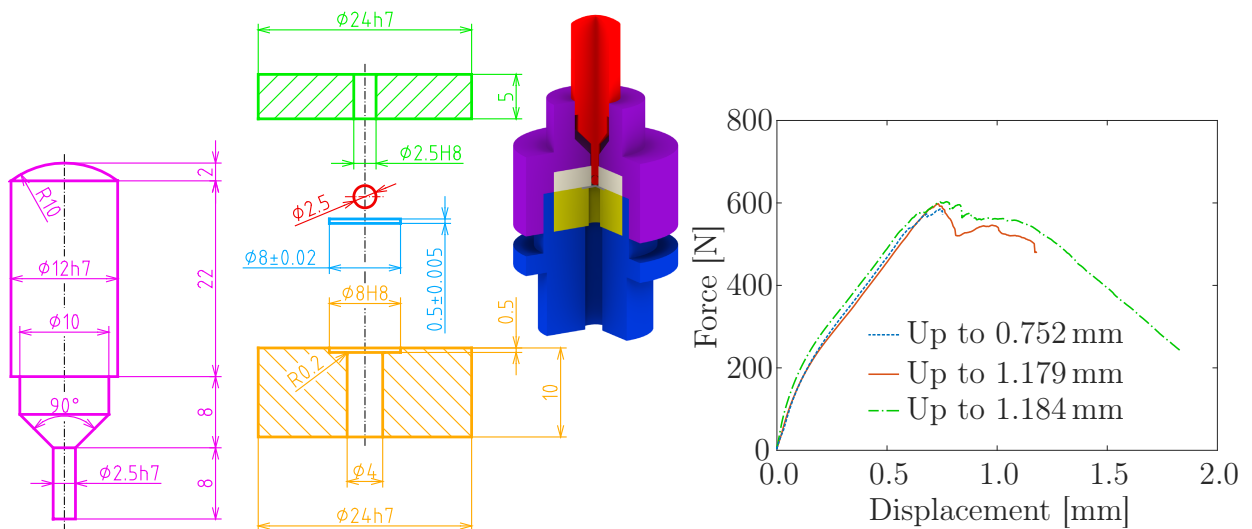


Figure 4.1: Small punch testing apparatus and responses from experiments (the final punch displacements are approximate)

The time of the simulation was 0.1 s, while the mass scaling with the time increment of  $1 \times 10^{-7}$  s was introduced in order to save some computational time. The kinetic energy was negligible when compared to the total one, so the quasi-static loading was maintained. The specimen was discretized with C3D8R elements having the characteristic size of 0.075 mm in the central zone (Fig. 4.2). The ball and tools were meshed with R3D4 elements with the characteristic size of 0.025 mm. The friction coefficient of 0.1 was used after the numerical analysis of its role.

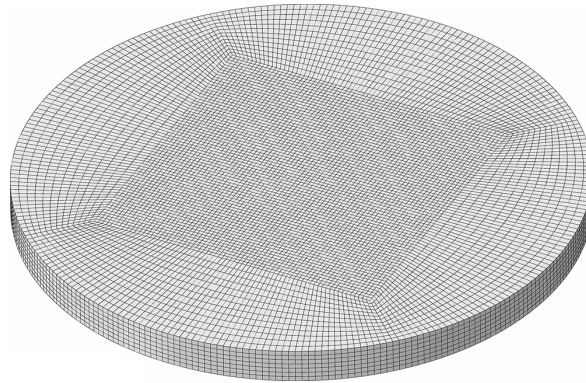


Figure 4.2: Mesh layout for the small punch test specimen

The experimental and computational responses (Fig. 4.3) represent a quantitative measure. As the results were obtained, the Lou–Huh criterion was recalibrated with a constraint  $\eta_c = -1$  at  $\xi = -1$  with consequently more severely overpredicting the experimental force response unfortunately. Even worse result was achieved when the calibration was carried out again, but without any constraint this time. It yielded in an unreal cut-off stress triaxiality around  $-8 \times 10^4$ , but quite surprisingly in a fit better approximately by 10% in total when compared to the results in Table 3.10. On the other hand, extended Mohr–Coulomb and KHPS2 criteria underpredicted the maximum force.

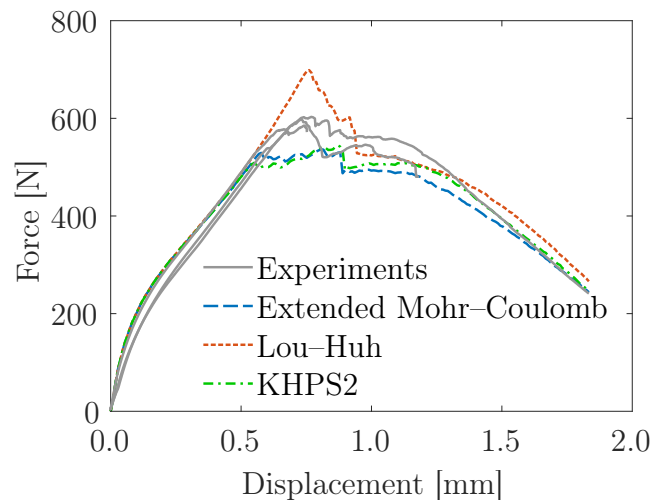


Figure 4.3: Experimental and computational force responses for the small punch testing

The fracture surfaces in Fig. 4.4 correspond to the three specimens that were tested. The observations were made after conducting the tests with the use of the field emission SEM ZEISS Ultra Plus equipped with an auto-emission cathode [101].

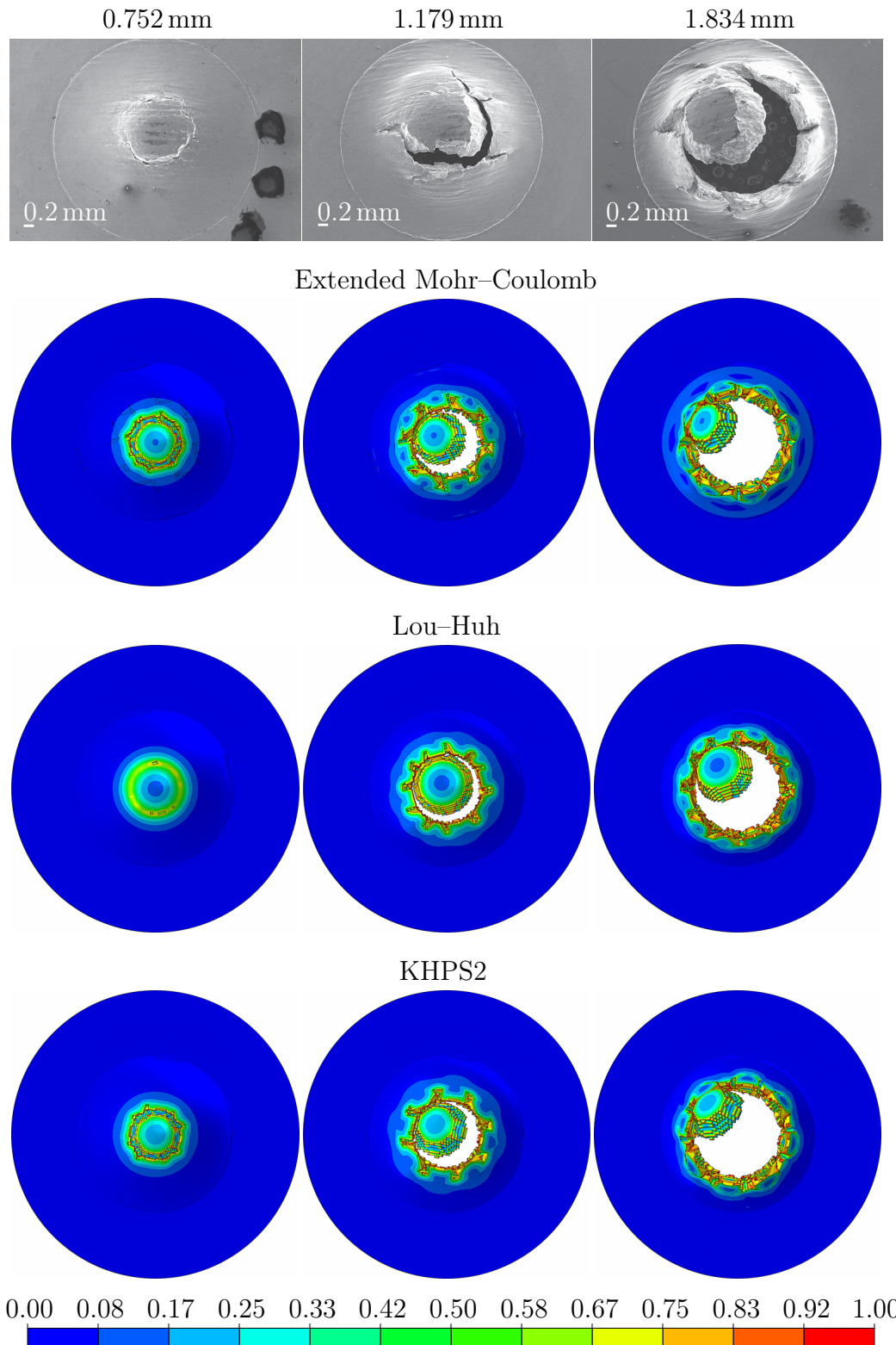


Figure 4.4: Damage parameter fields compared to the experimental obtained micrographs

The qualitative comparison was addressed by means of the fracture surfaces (Fig. 4.4). All the computational fracture surfaces were obtained from three different moments corresponding to the respective punch displacements. The extended Mohr–Coulomb and KHPS2 criteria performed in a similar manner. Lou–Huh criterion predicted more radial cracks and late cracking, which is apparent especially for the punch displacement of 0.752 mm (Fig. 4.4). Similar amount of elements was removed by all the criteria.

All the results presented here are quite similar to those obtained with simpler yield criterion by Šebek et al. [101].

## 4.2 Three-point bending

The three-point bending was another test for the validation of calibrated criteria. Zwick Z250 Allround-Line, tCII, with the Zwick multiXtens extensometer and loading rate of 2 mm/min were employed. The specimen had several randomly located notches, which caused a non-symmetrical deflection. The detailed drawing is in Fig. 4.5 along with the force responses of the two specimens. The punch had a radius of 5 mm. The supports had the span of 160 mm and same radii as the punch. The specimens were placed on the supports so that the bigger hole was centred [99].

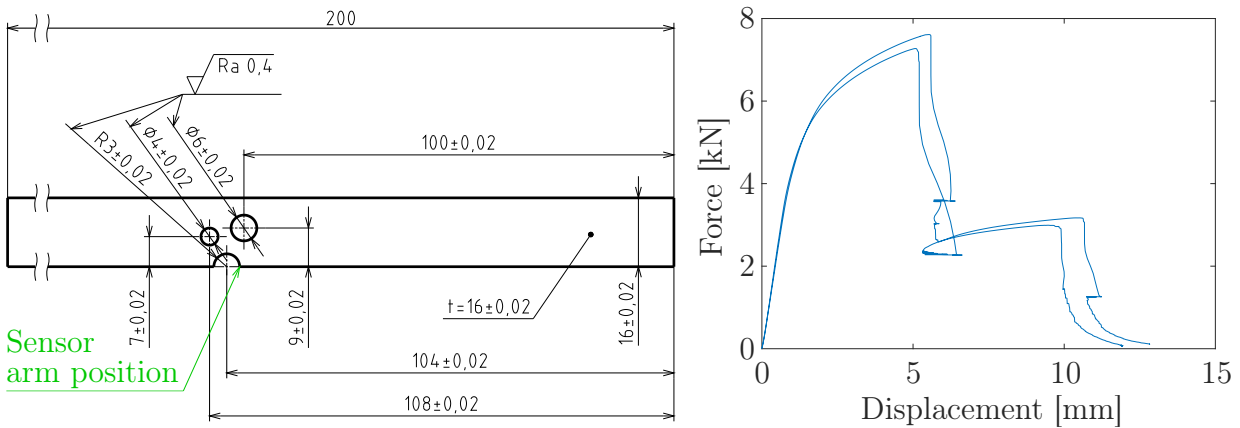


Figure 4.5: Drawing and responses of the three-point bending

The first sensor arm was stationary and touching the fixed testing machine frame, while the second sensor arm was placed on the edge of the surface notch closer to the larger hole, as highlighted in Fig. 4.5. A bouncing of the sensor arm was observed on the force–displacement responses. It occurred immediately after the rupture, when the energy was released and the crack propagated. The bounce can be recognized by the part of the responses, where the displacement is decreasing, which would be irrational otherwise. It should be noted that the bouncing of the sensor arm was captured by the optical measurement described later as well.

The crack initiated at the notch surface location I, as depicted in Fig. 4.6. It propagated laterally and inwards the material along the path II until the first section failed. After some additional loading, the secondary cracking initiated at the notch surface location III and propagated the same way as in the case of first cracking. The lateral rupture was finalized with the shear lips (Fig. 4.6).



Figure 4.6: Fractured specimens after the three-point bending test [99]

Again, the C3D8R element was deployed with the characteristic size of 0.075 mm in the regions of potential cracking. These regions with mapped mesh were surrounded by a free mesh with a characteristic element size of 0.2 mm, which finally transformed into the structured coarse mesh of 2 mm characteristic element size in the remote areas (Fig. 4.7). The characteristic element size of 0.075 mm was along the width everywhere. The punch and supports were modelled as rigid bodies with R3D4 elements. The punch had the characteristic size of 0.075 mm and the supports had the same size along the width, but 0.5 mm in the circumferential direction. There were approximately two millions of nodes in total. The simulation time was 0.1 s. There was a sudden drop in forces for this bi-failure test, which could lead to some oscillations. In order to avoid excessive vibrations, the time increment of  $5 \times 10^{-8}$  s was enforced – that is twice lower than in other simulations where the mass scaling was deployed, but still providing a sufficient decrease of the computational time, which was several weeks using the standard personal computer. The punch had a prescribed velocity on the contrary to other simulations, where the displacements and rotations were exploited. It should be noted that no symmetry was used, as in the case of small punch testing.

The force responses are compared in Fig. 4.8. It is clear that the extended Mohr–Coulomb criterion predicted the failure of the first section slightly earlier. Then, the computationally predicted responses were still captured well for the continuing loading until the onset of final rupture, where the crack initiation was predicted late by the Lou–Huh criterion. Nevertheless, all the criteria predicted very slow crack growth, while the secondary cracking was rapid in experiments, as in the case of the first failure. Moreover, the shocks may be traced in the force responses occurring after the first cracking, when a sudden drop of force appeared. These are due to the dynamic nature of the crack propagation and its representation by the explicit finite element calculation algorithm. Sudden change from a quasi-static behaviour to the dynamic propagation is followed by the parasitic oscillations, which could be treated only at the expense of much higher computational demands.

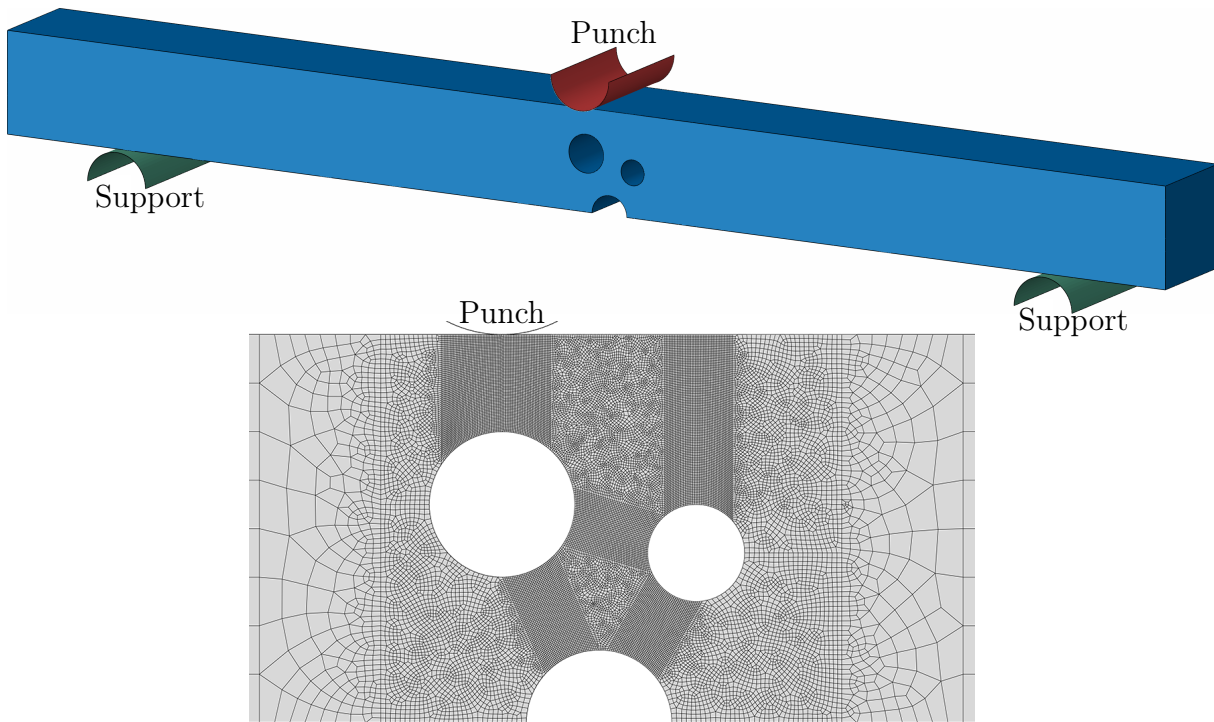


Figure 4.7: Assembly and detail of meshed notched block for the three-point bending

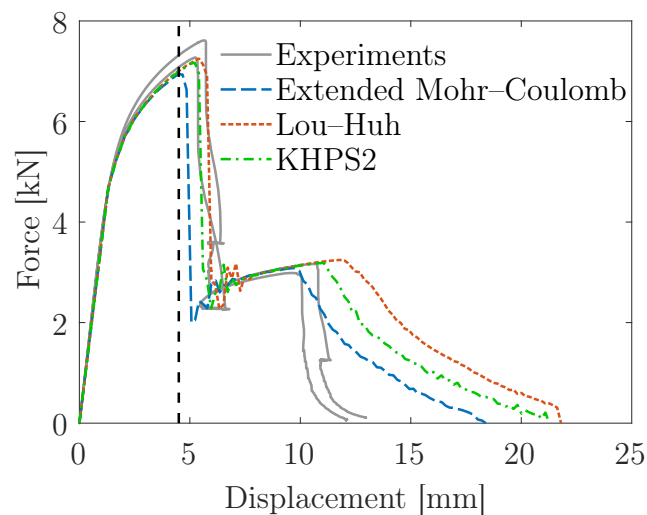


Figure 4.8: Three-point bending force responses from computations and experiments

The fracture surfaces from experiment and numerical simulations are displayed in Fig. 4.9. It is clear that no slant fracture was predicted by the KHPS2 criterion. It was captured by the extended Mohr-Coulomb and Lou-Huh criteria, but only in the first stage of cracking. Moreover, the computationally predicted shear lips were smaller than those observed experimentally. Additionally, the Lou-Huh criterion exhibited some unusual crack propagation in the final stage of cracking forming a shallow groove.

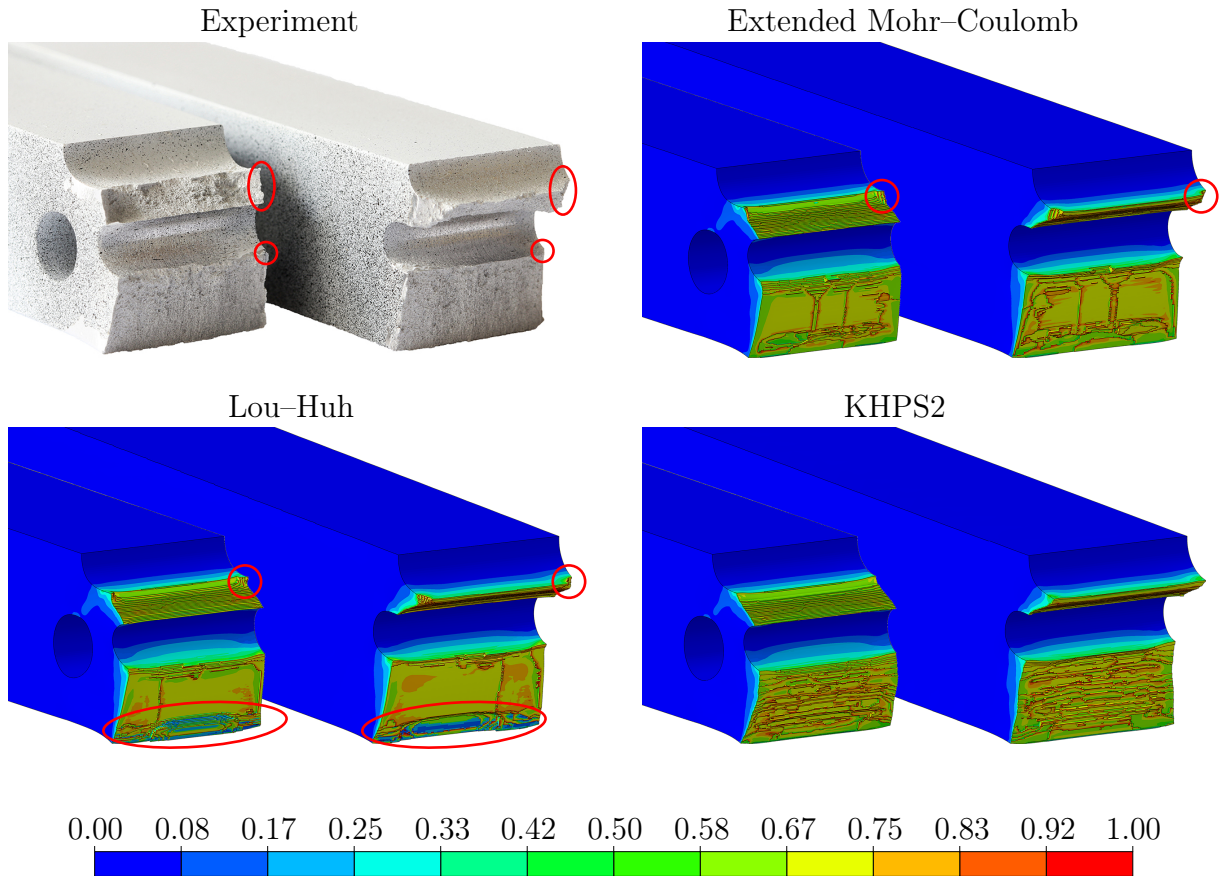


Figure 4.9: Fracture surfaces from experiments compared to those obtained computationally, where the field of damage parameter is displayed

There is a significant difference, when compared to Kubík et al. [99], who used a simpler plasticity model – Kroon–Faleskog yield criterion – with almost the same fracture criteria (there are slight differences in formulation of extended Mohr–Coulomb and Lou–Huh criteria) and reported much pronounced shear lips closer to reality and even in the second stage of cracking. On the other hand, it seems to be a trade-off as the accuracy in force responses was worse, which is probably given by less accurate model of plasticity, which probably influenced quite surprisingly the appearance of fracture surfaces extensively, while still not being that different from Bai–Wierzbicki yield criterion, see Subsection 3.2.5.

Last but not least, the digital image correlation was done in order to evaluate the model performance. The test was recorded by the mono digital camera Basler acA2000-165um with a resolution of  $2048 \times 1088$  px. The images were captured with a frame rate of 10 fps. A speckle pattern was created on the surface by the black spray on the white background so that the displacements could be calculated with Mercury RT x64 2.6. The grid spacing was 3 px, while the size of 1 px was 0.058 mm. This validation concerns mainly the plasticity as it was executed prior to the fracture. The contours may look the same for all the cases in Fig. 4.10, but there are minor differences due to the coupled approach, where damage and plasticity mutually influence each other. There was a good conformity between the experimental observation and calculations for the instant corresponding to the deflection of 4.5 mm (highlighted by the vertical black dashed line in Fig. 4.8).

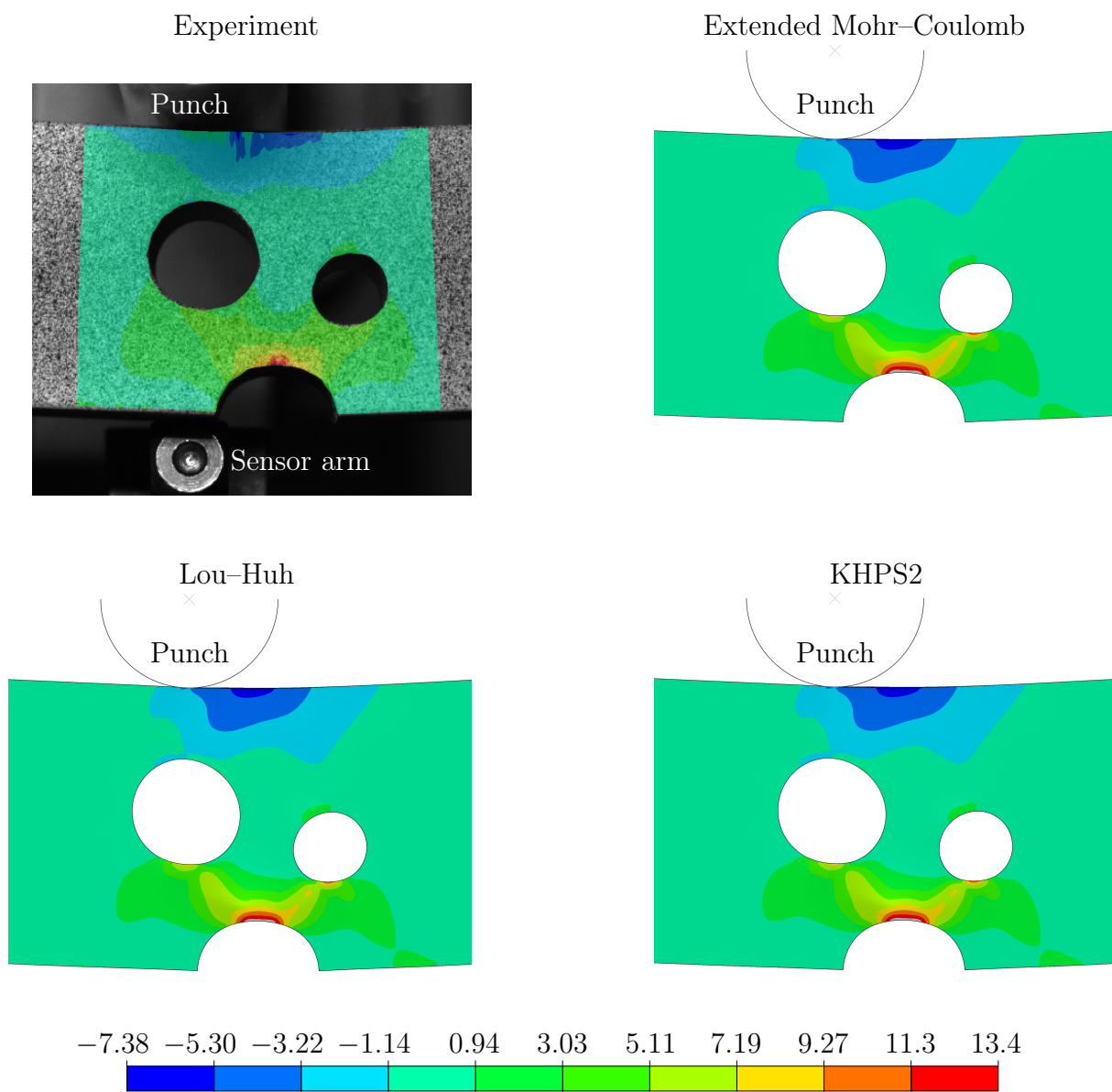


Figure 4.10: Field of horizontal strain component in percent obtained using the digital image correlation from the experiment compared to the numerical simulations

## 5 Conclusions

The present thesis deals with the ductile fracture under quasi-static monotonic loading and room temperature. The aluminium alloy 2024-T351 was studied. It was found that it is pressure and Lode dependent both for the plasticity as well as failure. Two Lode dependent plasticity yield criteria were calibrated, but the one with pressure dependency resulted in better responses, when compared to the experiments. Then, the non-linear damage accumulation law was calibrated by means of loading–unloading (semi-cyclic) tests of smooth cylindrical specimens. Finally, three ductile fracture criteria were calibrated towards the six experiments covering the tensile notched cylindrical specimens, tensile and torsional notched tubular specimens and upsetting notched cylindrical specimen, which was uniquely designed for that purpose. It was found that the latter experiment successfully substituted the classical compression test, which exhibits highly non-proportional evolution of the state variables in the crack initiation location. Moreover, the onset of fracture is very difficult to localize due to the barrelling of the smooth cylinder and presence of the friction on its faces. The non-proportionality may distort the results, when such affected state variables were used for the calibration of ductile fracture criteria, which was omitted in the present thesis.

The final part of this work focuses on a successful application of the calibrated models on the two distinct tests. It constitutes from the small punch testing and three-point bending. Computations of the first test revealed a good conformity with experiments regarding both the quantitative as well as qualitative measures. The latter of the two validation tests was more complicated as it exhibited a bi-failure mode of rupture. The force responses of the three-point bending were in a very good correspondence with the experimental observation, so as the fracture surfaces and the strains evaluated by the digital image correlation on the specimen’s surface prior to the first cracking onset.

### 5.1 Future studies

There are several things, which might be improved in the future. The ductile fracture criteria may be calibrated more reliably, when the tensile flat grooved specimens were included. This can cover the pressure dependency for the generalized shear more thoroughly. Then, the problem with predicted Lode dependency may arise, when the non-quadratic yield criterion was used. The predicted stress state is crucial as it serves as an input into the calibration procedure. However, it could be solved by implementation of non-associated flow rule [138]. Moreover, it could also help with better prediction of deformations, which might be unnaturally distorted with non-quadratic yield criterion [139].

The material anisotropy could be reflected in the yield criterion too. Then, it may explain the scatter in results across the publications, where the isotropic behaviour was adopted for the finite element modelling. Nevertheless, then the model becomes much more complicated.

There is another issue, as briefly discussed before, which arises due to the utilization of a coupled approach, when the plasticity is influenced by the damage accumulation via the flow curve softening. The problem is the loss of ellipticity and subsequent mesh dependency leading to the localization of the field variables disregarding the element size. This could be successfully solved in a way presented by Nguyen et al. [140] for example.

Last but not least, the more reliable experimental tracking of the damage accumulation can be realized, as discussed in detail earlier. This can involve the non-proportional biaxial loading of notched tubular specimens or better of the cruciform specimens. The present loading–unloading technique, which was utilized here, was originally developed for a different group of models in the scope of continuum damage mechanics. Therefore, more physically sound background is needed.

## References

- [1] CERIK, B. C., K. LEE, S.-J. PARK and J. CHOUNG. Simulation of ship collision and grounding damage using Hosford-Coulomb fracture model for shell elements. *Ocean Engineering*. 2019, **173**, 415–432.
- [2] TALEMI, R., S. COOREMAN, H. MAHGEREFTEH, S. MARTYNOV and S. BROWN. A fully coupled fluid-structure interaction simulation of three-dimensional dynamic ductile fracture in a steel pipeline. *Theoretical and Applied Fracture Mechanics*. 2019, **101**, 224–235.
- [3] ŠEBEK, F., P. KUBÍK and J. PETRUŠKA. Prediction of central bursting in the process of forward extrusion using the uncoupled ductile failure models. *Advances in Materials and Processing Technologies*. 2015, **1**(1–2), 43–48.
- [4] GACHET, J.-M., G. DELATTRE and P.-O. BOUCHARD. Improved fracture criterion to chain forming stage and in use mechanical strength computations of metallic parts – Application to half-blanked components. *Journal of Materials Processing Technology*. 2015, **216**, 260–277.
- [5] LIST, G., G. SUTTER and A. BOUTHICHE. Cutting temperature prediction in high speed machining by numerical modelling of chip formation and its dependence with crater wear. *International Journal of Machine Tools and Manufacture*. 2012, **54–55**, 1–9.
- [6] WANG, B. and Z. LIU. Evaluation on fracture locus of serrated chip generation with stress triaxiality in high speed machining of Ti6Al4V. *Materials & Design*. 2016, **98**, 68–78.
- [7] ŠEBEK, F., P. KUBÍK, J. PETRUŠKA and J. HŮLKA. Extremely low-stress triaxiality tests in calibration of fracture models in metal-cutting simulation. *Metallurgical and Materials Transactions A*. 2016, **47**(11), 5302–5312.
- [8] MANAHAN, M. P., A. S. ARGON and O. K. HARLING. The development of a miniaturized disk bend test for the determination of postirradiation mechanical properties. *Journal of Nuclear Materials*. 1981, **104**, 1545–1550.
- [9] XIAO, X., W. YAOPEI, V. V. VERSHININ, L. CHEN and Y. LOU. Effect of Lode angle in predicting the ballistic resistance of Weldox 700 E steel plates struck by blunt projectiles. *International Journal of Impact Engineering*. 2019, **128**, 46–71.

- [10] KRAMER, S. L. B., A. JONES, A. MOSTAFA, B. RAVAJI, T. TANCOGNE-DEJEAN, Ch. C. ROTH, M. B. GORJI, K. PACK, J. T. FOSTER, M. BEHZAD-INASAB, J. C. SOBOTKA, J. M. MCFARLAND, J. STEIN, A. D. SPEAR, P. NEWELL, M. W. CZABAJ, B. WILLIAMS, H. SIMHA, M. GESING, L. N. GILKEY, Ch. A. JONES, R. DINGEREVILLE, S. E. SANBORN, J. L. BIGNELL, A. R. CERRONE, V. KEIM, A. NONN, S. COOREMAN, P. THIBAUX, N. AMES, D. O. CONNOR, M. PARNO, B. DAVIS, J. TUCKER, B. COUDRILLIER, K. N. KARLSON, J. T. OSTIEN, J. W. FOULK III, Ch. I. HAMMETTER, S. GRANGE, J. M. EMERY, J. A. BROWN, J. E. BISHOP, K. L. JOHNSON, K. R. FORD, S. BRINCKMANN, M. K. NEILSEN, J. JACKIEWICZ, K. RAVICHANDAR, T. IVANOFF, B. C. SALZBRENNER and B. L. BOYCE. The third Sandia fracture challenge: Predictions of ductile fracture in additively manufactured metal. *International Journal of Fracture*. 2019, **218**, 5–61.
- [11] ERICE, B., Ch. C. ROTH and D. MOHR. Stress-state and strain-rate dependent ductile fracture of dual and complex phase steel. *Mechanics of Materials*. 2018, **116**, 11–32.
- [12] PARK, N., H. HUH and J. W. YOON. Anisotropic fracture forming limit diagram considering non-directionality of the equi-biaxial fracture strain. *International Journal of Solids and Structures*. 2018, **151**, 181–194.
- [13] ROTH, Ch. C., T. F. MORGENEYER, Y. CHENG, L. HELFEN and D. MOHR. Ductile damage mechanism under shear-dominated loading: In-situ tomography experiments on dual phase steel and localization analysis. *International Journal of Plasticity*. 2018, **109**, 169–192.
- [14] LIN, J., Y. HOU, J. MIN, H. TANG, J. E. CARSLEY and T. B. STOUGHTON. Effect of constitutive model on springback prediction of MP980 and AA6022-T4. *International Journal of Material Forming*. 2020, **13**, 1–13.
- [15] LEE, E.-H., H. CHOI, T. B. STOUGHTON and J. W. YOON. Combined anisotropic and distortion hardening to describe directional response with Bauschinger effect. *International Journal of Plasticity*. 2019, **122**, 73–88.
- [16] BOUDIFA, M., K. SAANOUNI and J.-L. CHABOCHE. A micromechanical model for inelastic ductile damage prediction in polycrystalline metals for metal forming. *International Journal of Mechanical Sciences*. 2009, **51**(6), 453–464.
- [17] SCHERER, J. M., J. BESSON, S. FOREST, J. HURE and B. TANGUY. Strain gradient crystal plasticity with evolving length scale: Application to voided irradiated materials. *European Journal of Mechanics - A/Solids*. 2019, **77**, 103768.
- [18] TANCOGNE-DEJEAN, T., M. B. GORJI, K. PACK and Ch. C. ROTH. The third Sandia Fracture Challenge: Deterministic and probabilistic modeling of ductile fracture of additively-manufactured material. *International Journal of Fracture*. 2019, **218**, 209–229.

- [19] KOMORI, K. Simulation of shearing by node separation method. *Computers & Structures*. 2001, **79**(2), 197–207.
- [20] VAUCORBEIL, de A. and Ch. R. HUTCHINSON. A new total-Lagrangian smooth particle hydrodynamics approximation for the simulation of damage and fracture of ductile materials. *International Journal for Numerical Methods in Engineering*. 2020, **121**(10), 2227–2245.
- [21] SEABRA, M. R. R., P. ŠUŠTARIČ, J. M. A. CESAR DE SA and T. RODIČ. Damage driven crack initiation and propagation in ductile metals using XFEM. *Computational Mechanics*. 2013, **52**, 161–179.
- [22] TVERGAARD, V. Influence of voids on shear band instabilities under plane strain conditions. *International Journal of Fracture*. 1981, **17**(4), 389–407.
- [23] TVERGAARD, V. On localization in ductile materials containing spherical voids. *International Journal of Fracture*. 1982, **18**(4), 237–252.
- [24] TVERGAARD, V. and A. NEEDLEMAN. Analysis of the cup-cone fracture in a round tensile bar. *Acta Metallurgica*. 1984, **32**(1), 157–169.
- [25] DUGDALE, D. S. Yielding of steel sheets containing slits. *Journal of the Mechanics and Physics of Solids*. 1960, **8**(2), 100–104.
- [26] BARENBLATT, G. I. The mathematical theory of equilibrium cracks in brittle fracture. *Advances in Applied Mechanics*. 1962, **7**, 55–129.
- [27] LODE, von W. Versuche über den Einfluß der mittleren Hauptspannung auf die Fließgrenze. *Zeitschrift für Angewandte Mathematik und Mechanik*. 1925, **5**(2), 142–144.
- [28] WU, C. T. and B. REN. A stabilized non-ordinary state-based peridynamics for the nonlocal ductile material failure analysis in metal machining process. *Computer Methods in Applied Mechanics and Engineering*. 2015, **291**, 197–215.
- [29] WILKINS, M. L., R. D. STREIT and J. E. REAUGH. *Cumulative-strain-damage model of ductile fracture: Simulation and prediction of engineering fracture tests*. Livermore: Lawrence Livermore National Laboratory, 1980.
- [30] BRIDGMAN, P. W. *Studies in large plastic flow and fracture: With special emphasis on the effects of hydrostatic pressure*. Cambridge, Harvard University Press, 1964.
- [31] COCKROFT, M. G. and D. J. LATHAM. Ductility and the workability of metals. *Journal of the Institute of Metals*. 1968, **96**, 33–39.
- [32] BROZZO, P., B. DELUCA and R. RENDINA. A new method for the prediction of formability limits in metal sheets. In *Proceedings of the 7th Biennial Conference of the International Deep Drawing Research Group*. Amsterdam, 1972, pp. 3.1–3.5.

- [33] OH, S. I., C. C. CHEN and S. KOBAYASHI. Ductile fracture in axisymmetric extrusion and drawing: Part 2—Workability in extrusion and drawing. *Journal of Engineering for Industry*. 1979, **101**(1), 36–44.
- [34] KO, Y. K., J. S. LEE, H. HUH, H. K. KIM and S. H. PARK. Prediction of fracture in hub-hole expanding process using a new ductile fracture criterion. *Journal of Materials Processing Technology*. 2007, **187–188**, 358–362.
- [35] RICE, J. R. and D. M. TRACEY. On the ductile enlargement of voids in triaxial stress fields. *Journal of the Mechanics and Physics of Solids*. 1969, **17**(3), 201–217.
- [36] MCCLINTOCK, F. A. A criterion for ductile fracture by the growth of holes. *Journal of Applied Mechanics*. 1968, **35**(2), 363–371.
- [37] JOHNSON, G. R. and W. H. COOK. Fracture characteristics of three metals subjected to various strains, strain rates, temperatures and pressures. *Engineering Fracture Mechanics*. 1985, **21**(1), 31–48.
- [38] JOHNSON, G. R. Materials characterization for computations involving severe dynamic loadings. In *Designing for Extremes: Environment, Loading, and Structural Behavior*. Watertown: Army Materials and Mechanics Research Center, 1980, pp. 62–67.
- [39] BAO, Y. and T. WIERZBICKI. On fracture locus in the equivalent strain and stress triaxiality space. *International Journal of Mechanical Sciences*. 2004, **46**(1), 81–98.
- [40] BAO, Y. *Prediction of ductile crack formation in uncracked bodies*. Cambridge, 2003. PhD Thesis. Massachusetts Institute of Technology.
- [41] XUE, L. Constitutive modeling of void shearing effect in ductile fracture of porous materials. *Engineering Fracture Mechanics*. 2008, **75**(11), 3343–3366.
- [42] WIERZBICKI, T., Y. BAO, Y.-W. LEE and Y. BAI. Calibration and evaluation of seven fracture models. *International Journal of Mechanical Sciences*. 2005, **47**(4–5), 719–743.
- [43] BAI, Y. and T. WIERZBICKI. A new model of metal plasticity and fracture with pressure and Lode dependence. *International Journal of Plasticity*. 2008, **24**(6), 1071–1096.
- [44] BAI, Y. *Effect of loading history on necking and fracture*. Cambridge, 2008. PhD Thesis. Massachusetts Institute of Technology.
- [45] BAI, Y. and T. WIERZBICKI. Application of extended Mohr–Coulomb criterion to ductile fracture. *International Journal of Fracture*. 2010, **161**(1), 1–20.
- [46] HOLLOMON, J. H. Tensile deformation. *Metals Technology*. 1945, 268–290.
- [47] LOU, Y., H. HUH, S. LIM and K. PACK. New ductile fracture criterion for prediction of fracture forming limit diagrams of sheet metals. *International Journal of Solids and Structures*. 2012, **49**(25), 3605–3615.

- [48] LOU, Y. and H. HUH. Extension of a shear-controlled ductile fracture model considering the stress triaxiality and the Lode parameter. *International Journal of Solids and Structures*. 2013, **50**(2), 447–455.
- [49] LOU, Y., J. W. YOON and H. HUH. Modeling of shear ductile fracture considering a changeable cut-off value for stress triaxiality. *International Journal of Plasticity*. 2014, **54**, 56–80.
- [50] LOU, Y. *A new ductile fracture criterion for the formability prediction of steel sheets and its application to finite element analysis*. Daejeon, 2012. PhD Thesis. KAIST.
- [51] KUBÍK, P., F. ŠEBEK and J. PETRUŠKA. Notched specimen under compression for ductile failure criteria. *Mechanics of Materials*. 2018, **125**, 94–109.
- [52] XIAO, X., Z. MU, H. PAN and Y. LOU. Effect of the Lode parameter in predicting shear cracking of 2024-T351 aluminum alloy Taylor rods. *International Journal of Impact Engineering*. 2018, **120**, 185–201.
- [53] LOU, Y., L. CHEN, T. CLAUSMEYER, A. ERMAN TEKKAYA and Y. J. YOON. Modeling of ductile fracture from shear to balanced biaxial tension for sheet metals. *International Journal of Solids and Structures*. 2017, **112**, 169–184.
- [54] LOU, Y. and J. W. YOON. Anisotropic ductile fracture criterion based on linear transformation. *International Journal of Plasticity*. 2017, **93**, 3–25.
- [55] ROTH, Ch. C. and D. MOHR. Effect of strain rate on ductile fracture initiation in advanced high strength steel sheets: Experiments and modeling. *International Journal of Plasticity*. 2014, **56**, 19–44.
- [56] KACHANOV, L. M. Rupture time under creep conditions. *Izvestia Akademii Nauk SSSR, Otdelenie Tekhnicheskich Nauk*. 1958, (8), 26–31.
- [57] RABOTNOV, Y. N. On the equations of state for creep. *Progress in Applied Mechanics*. 1963, **the Prager Anniversary Volume**, 307–315.
- [58] ROUSSELIER, G. *An experimental and analytical study of ductile fracture and stable crack-growth*. Daresbury: International Energy Agency, 1978, pp. 14.1–14.5.
- [59] GURSON, A. L. *Plastic flow and fracture behavior of ductile materials incorporating void nucleation, growth, and interaction*. Providence, 1975. PhD Thesis. Brown University.
- [60] GURSON, A. L. *Continuum theory of ductile rupture by void nucleation and growth: Part I - Yield criteria and flow rules for porous ductile media*. Providence: Brown University, 1975.
- [61] GURSON, A. L. Continuum theory of ductile rupture by void nucleation and growth: Part I—Yield criteria and flow rules for porous ductile media. *Journal of Engineering Materials and Technology*. 1977, **99**(1), 2–15.

- [62] KRAJČINOVIC, D. and G. U. FONSEKA. The continuous damage theory of brittle materials, Part 1: General theory. *Journal of Applied Mechanics*. 1981, **48**(4), 809–815.
- [63] KRAJČINOVIC, D. Constitutive equations for damaging materials. *Journal of Applied Mechanics*. 1983, **50**(2), 355–360.
- [64] LEMAITRE, J. Coupled elasto-plasticity and damage constitutive equations. *Computer Methods in Applied Mechanics and Engineering*. 1985, **51**, 31–49.
- [65] LEMAITRE, J. A continuous damage mechanics model for ductile fracture. *Journal of Engineering Materials and Technology*. 1985, **107**(1), 83–89.
- [66] CHABOCHE, J.-L. Continuum damage mechanics: Part I—General concepts. *Journal of Applied Mechanics*. 1988, **55**(1), 59–64.
- [67] SAANOUNI, K., Ch. FOSTER and F. B. HATIRA. On the anelastic flow with damage. *International Journal of Damage Mechanics*. 1994, **3**(2), 140–169.
- [68] BONORA, N. A nonlinear CDM model for ductile failure. *Engineering Fracture Mechanics*. 1997, **58**(1–2), 11–28.
- [69] BØRVIK, T., O. S. HOPPERSTAD, T. BERSTAD and M. LANGSETH. A computational model of viscoplasticity and ductile damage for impact and penetration. *European Journal of Mechanics - A/Solids*. 2001, **20**(5), 685–712.
- [70] SOYARSLAN, C., A. E. TEKKAYA and U. AKYUZ. Application of Continuum Damage Mechanics in discontinuous crack formation: Forward extrusion chevron predictions. *Zeitschrift für Angewandte Mathematik und Mechanik*. 2008, **88**(6), 436–453.
- [71] SIDOROFF, F. Description of anisotropic damage application to elasticity. In *Physical Non-Linearities in Structural Analysis*. Berlin: Springer-Verlag, 1981, pp. 237–244. ISBN: 978-3-642-81584-3.
- [72] CHABOCHE, J.-L. Continuous damage mechanics — A tool to describe phenomena before crack initiation. *Nuclear Engineering and Design*. 1981, **64**(2), 233–247.
- [73] MURAKAMI, S. and N. OHNO. A continuum theory of creep and creep damage. In *Creep in Structures*. Berlin: Springer-Verlag, 1981, pp. 422–444. ISBN: 978-3-642-81600-0.
- [74] CHOW, C. L. and J. WANG. An anisotropic theory of elasticity for continuum damage mechanics. *International Journal of Fracture*. 1987, **33**, 3–16.
- [75] LEMAITRE, J., R. DESMORAT and M. SAUZAY. Anisotropic damage law of evolution. *European Journal of Mechanics - A/Solids*. 2000, **19**(2), 187–208.
- [76] BRÜNIG, M. Numerical analysis and elastic–plastic deformation behavior of anisotropically damaged solids. *International Journal of Plasticity*. 2002, **18**(9), 1237–1270.

- [77] BESSON, J. Continuum models of ductile fracture: A review. *International Journal of Damage Mechanics*. 2010, **19**(1), 3–52.
- [78] KATTAN, P. I. and G. Z. VOYIADJIS. Decomposition of damage tensor in continuum damage mechanics. *Journal of Engineering Mechanics*. 2001, **127**(9), 940–944.
- [79] XUE, L. Damage accumulation and fracture initiation in uncracked ductile solids subject to triaxial loading. *International Journal of Solids and Structures*. 2007, **44**(16), 5163–5181.
- [80] ŠEBEK, F. *Ductile fracture criteria in multiaxial loading – Theory, experiments and application*. Brno, 2016. PhD Thesis. Brno University of Technology.
- [81] LI, Y. and T. WIERZBICKI. Prediction of plane strain fracture of AHSS sheets with post-initiation softening. *International Journal of Solids and Structures*. 2010, **47**(17), 2316–2327.
- [82] BEESE, A. M., M. LUO, Y. LI, Y. BAI and T. WIERZBICKI. Partially coupled anisotropic fracture model for aluminum sheets. *Engineering Fracture Mechanics*. 2010, **77**(7), 1128–1152.
- [83] BAI, Y. and T. ATKINS. Tension and shear cracking during indentation of ductile materials by opposed wedges. *Engineering Fracture Mechanics*. 2012, **96**, 49–60.
- [84] PAREDES, M., D. F. B. SARZOSA, R. SAVIOLI, T. WIERZBICKI, D. Y. JEONG and D. C. TYRELL. Ductile tearing analysis of TC128 tank car steel under mode I loading condition. *Theoretical and Applied Fracture Mechanics*. 2018, **96**, 658–675.
- [85] KEIM, V., M. PAREDES, A. NONN and S. MÜNSTERMANN. FSI-simulation of ductile fracture propagation and arrest in pipelines: Comparison with existing data of full-scale burst tests. *International Journal of Pressure Vessels and Piping*. 2020, **182**, 104067.
- [86] SEIDENFUSS, M., M. K. SAMAL and E. ROOS. On critical assessment of the use of local and nonlocal damage models for prediction of ductile crack growth and crack path in various loading and boundary conditions. *International Journal of Solids and Structures*. 2011, **48**(24), 3365–3381.
- [87] ANDRADE, F. X. C., J. M. A. CÉSAR DE SÁ and F. M. ANDRADE PIRES. A ductile damage nonlocal model of integral-type at finite strains: Formulation and numerical issues. *International Journal of Damage Mechanics*. 2011, **20**(4), 515–557.
- [88] BALTIC, S., J. MAGNIEN, H.-P. GÄNSER, T. ANTRETTTER and R. HAMMER. Coupled damage variable based on fracture locus: Modelling and calibration. *International Journal of Plasticity*. 2020, **126**, 102623.
- [89] BAO, Y. Dependence of fracture ductility on thickness. *Thin-Walled Structures*. 2004, **42**(8), 1211–1230.

- [90] PAPANIDERO, J., V. DOQUET and S. LEPEER. Multiscale investigation of ductile fracture mechanisms and strain localization under shear loading in 2024-T351 aluminum alloy and 36NiCrMo16 steel. *Materials Science and Engineering: A*. 2014, **610**, 203–219.
- [91] HARTLEN, D. C. and D. A. DOMAN. A constitutive model fitting methodology for ductile metals using cold upsetting tests and numeric optimization techniques. *Journal of Engineering Materials and Technology*. 2019, **141**(1), 011008.
- [92] KHAN, A. S. and H. LIU. A new approach for ductile fracture prediction on Al 2024-T351 alloy. *International Journal of Plasticity*. 2012, **35**, 1–12.
- [93] QUACH, H., J.-J. KIM, D.-C. NGUYEN and Y.-S. KIM. Uncoupled ductile fracture criterion considering secondary void band behaviors for failure prediction in sheet metal forming. *International Journal of Mechanical Sciences*. 2020, **169**, 105297.
- [94] HUSSEY, R. J. and J. WILSON. *Light Alloys: Directory and Databook*. Boston: Springer US, 1998. ISBN: 978-0-412-80410-6.
- [95] BAI, Y., Y. BAO and T. WIERZBICKI. Fracture of prismatic aluminum tubes under reverse straining. *International Journal of Impact Engineering*. 2006, **32**(5), 671–701.
- [96] SEIDT, J. D. and A. GILAT. Plastic deformation of 2024-T351 aluminum plate over a wide range of loading conditions. *International Journal of Solids and Structures*. 2013, **50**(10), 1781–1790.
- [97] PAPANIDERO, J., V. DOQUET and D. MOHR. Ductile fracture of aluminum 2024-T351 under proportional and non-proportional multi-axial loading: Bao–Wierzbicki results revisited. *International Journal of Solids and Structures*. 2015, **69–70**, 459–474.
- [98] XIAO, X., H. PAO, Y. BAI, Y. LOU and L. CHEN. Application of the modified Mohr–Coulomb fracture criterion in predicting the ballistic resistance of 2024-T351 aluminum alloy plates impacted by blunt projectiles. *International Journal of Impact Engineering*. 2019, **123**, 26–37.
- [99] KUBÍK, P., F. ŠEBEK, J. ZAPLETAL, J. PETRUŠKA and T. NÁVRAT. Ductile failure predictions for the three-point bending test of a complex geometry made from aluminum alloy. *Journal of Engineering Materials and Technology*. 2019, **141**(4), 041011.
- [100] SEIDT, J. D. *Plastic deformation and ductile fracture of 2024-T351 aluminum under various loading conditions*. Columbus, 2010. PhD Thesis. The Ohio State University.
- [101] ŠEBEK, F., N. PARK, P. KUBÍK, J. PETRUŠKA and J. ZAPLETAL. Ductile fracture predictions in small punch testing of cold-rolled aluminium alloy. *Engineering Fracture Mechanics*. 2019, **206**, 509–525.

- [102] PARK, N., T. B. STOUGHTON and J. W. YOON. A new approach for fracture prediction considering general anisotropy of metal sheets. *International Journal of Plasticity*. 2020, **124**, 199–225.
- [103] LOU, Y., S. ZHANG and J. W. YOON. A reduced Yld2004 function for modeling of anisotropic plastic deformation of metals under triaxial loading. *International Journal of Mechanical Sciences*. 2019, **161–162**, 105027.
- [104] XUE, L. Stress based fracture envelope for damage plastic solids. *Engineering Fracture Mechanics*. 2009, **76**(3), 419–438.
- [105] PAPASIDERO, J., V. DOQUET and D. MOHR. Determination of the effect of stress state on the onset of ductile fracture through tension-torsion experiments. *Experimental Mechanics*. 2014, **54**, 137–151.
- [106] CHAI, R., Y. LOU and J. W. YOON. Assessment of newly developed ductile fracture criteria for lightweight metals. *Key Engineering Materials*. 2019, **794**, 42–47.
- [107] KWEON, S. Damage at negative triaxiality. *European Journal of Mechanics - A/Solids*. 2012, **31**(1), 203–212.
- [108] HALTOM, S. S., S. KYRIAKIDES and K. RAVI-CHANDAR. Ductile failure under combined shear and tension. *International Journal of Solids and Structures*. 2013, **50**(10), 1507–1522.
- [109] SCALES, M., N. TARDIF and S. KYRIAKIDES. Ductile failure of aluminum alloy tubes under combined torsion and tension. *International Journal of Solids and Structures*. 2016, **97–98**, 116–128.
- [110] LI, H., M. W. FU, J. LU and H. YANG. Ductile fracture: Experiments and computations. *International Journal of Plasticity*. 2011, **27**(2), 147–180.
- [111] CAO, T.-S., A. GAILLAC, P. MONTMITONNET and P.-O. BOUCHARD. Identification methodology and comparison of phenomenological ductile damage models via hybrid numerical–experimental analysis of fracture experiments conducted on a zirconium alloy. *International Journal of Solids and Structures*. 2013, **50**(24), 3984–3999.
- [112] HUBER, M. T. Właściwa praca odkształcenia jako miara wyężenia materiału. *Towarzystwo Politechniczne*. 1904, **22**, 38–81.
- [113] MISES, von R. Mechanik der festen Körpern im plastisch-deformablen Zustand. *Nachrichten von der Königlichen Gesellschaft der Wissenschaften zu Göttingen, Mathematisch-physikalische Klasse*. 1913, 582–592.
- [114] HENCKY, H. Zur Theorie plastischer Deformationen und der hierdurch im Material hervorgerufenen Nachspannungen. *Zeitschrift für angewandte Mathematik und Mechanik*. 1924, **4**(4), 323–334.

- [115] KROON, M. and J. FALESKOG. Numerical implementation of a  $J_2$ - and  $J_3$ -dependent plasticity model based on a spectral decomposition of the stress deviator. *Computational Mechanics*. 2013, **52**(5), 1059–1070.
- [116] TRESCA, M. H. Mémoire sur l'écoulement des corps solides soumis à de fortes pressions. *Compte Rendu des Séances de l'Académie des Sciences*. 1864, 754–758.
- [117] VERSHININ, V. V. A correct form of Bai–Wierzbicki plasticity model and its extension for strain rate and temperature dependence. *International Journal of Solids and Structures*. 2017, **126–127**, 150–162.
- [118] DRUCKER, D. C. and W. PRAGER. Soil mechanics and plastic analysis or limit design. *Quarterly Journal of Mechanics & Applied Mathematics*. 1952, **X**(2), 157–165.
- [119] LIAN, J., M. SHARAF, F. ARCHIE and S. MÜNSTERMANN. A hybrid approach for modelling of plasticity and failure behaviour of advanced high-strength steel sheets. *International Journal of Damage Mechanics*. 2013, **22**(2), 188–218.
- [120] FINCATO, R. and S. TSUTSUMI. Numerical modeling of the evolution of ductile damage under proportional and non-proportional loading. *International Journal of Solids and Structures*. 2019, **160**, 247–264.
- [121] LEMAITRE, J. and J. DUFAILY. Damage measurements. *Engineering Fracture Mechanics*. 1987, **28**(5–6), 643–661.
- [122] DERPENSKI, L., J. SZUSTA and A. SEWERYN. Damage accumulation and ductile fracture modeling of notched specimens under biaxial loading at room temperature. *International Journal of Solids and Structures*. 2018, **134**, 1–19.
- [123] BENZERGA, A. A., D. SUROVIK and S. M. KERALAVARMA. On the path-dependence of the fracture locus in ductile materials – Analysis. *International Journal of Plasticity*., 2012, **37**, 157–170.
- [124] BASU, S. and A. A. BENZERGA. On the path-dependence of the fracture locus in ductile materials: Experiments. *International Journal of Solids and Structures*. 2015, **71**, 79–90.
- [125] THOMAS, N., S. BASU and A. A. BENZERGA. On fracture loci of ductile materials under non-proportional loading. *International Journal of Mechanical Sciences*. 2016, **117**, 135–151.
- [126] CORTESE, L., F. NALLI and M. ROSSI. A nonlinear model for ductile damage accumulation under multiaxial non-proportional loading conditions. *International Journal of Plasticity*. 2016, **85**, 77–92.
- [127] BRÜNIG, M., S. GERKE and M. ZISTL. Experiments and numerical simulations with the H-specimen on damage and fracture of ductile metals under non-proportional loading paths. *Engineering Fracture Mechanics*. 2019, **217**, 106531.

- [128] GERKE, S., M. ZISTL, A. BHARDWAJ and M. BRÜNIG. Experiments with the X0-specimen on the effect of non-proportional loading paths on damage and fracture mechanisms in aluminum alloys. *International Journal of Solids and Structures*. 2019, **163**, 157–169.
- [129] GERKE, S., M. ZISTL and M. BRÜNIG. Experiments and numerical simulation of damage and fracture of the X0-specimen under non-proportional loading paths. *Engineering Fracture Mechanics*. 2020, **224**, 106795.
- [130] MANSON, S. S. and G. R. HALFORD. Re-examination of cumulative fatigue damage analysis—An engineering perspective. *Engineering Fracture Mechanics*. 1986, **25**(5–6), 539–571.
- [131] MANSON, S. S. and G. R. HALFORD. *Re-examination of cumulative fatigue damage analysis—An engineering perspective*. Cleveland: Lewis Research Center, 1985.
- [132] ŠEBEK, F., J. PETRUŠKA and P. KUBÍK. Lode dependent plasticity coupled with nonlinear damage accumulation for ductile fracture of aluminium alloy. *Materials & Design*. 2018, **137**, 90–107.
- [133] ŠEBEK, F., P. KUBÍK, J. HŮLKA and J. PETRUŠKA. Strain hardening exponent role in phenomenological ductile fracture criteria. *European Journal of Mechanics - A/Solids*. 2016, **57**, 149–164.
- [134] HŮLKA, J. *Computational prediction of ductile fracture*. Brno, 2014. PhD Thesis. Brno University of Technology.
- [135] KUBÍK, P., J. PETRUŠKA and J. HŮLKA. A new ductile fracture criterion of aluminium alloy. In *Modelling and Optimization of Physical Systems*. Gliwice: Wydawnictwo Katedry Mechaniki Teoretycznej i Stosowanej, 2013, pp. 43–46. ISBN: 83-60102-65-1.
- [136] GAO, X., G. ZHANG and Ch. ROE. A study on the effect of the stress state on ductile fracture. *International Journal of Damage Mechanics*. 2010, **19**(1), 75–94.
- [137] ŠEBEK, F., P. KUBÍK and J. PETRUŠKA. Standard tensile test compared to the small punch test of aluminium alloy. In *Engineering mechanics 2018*. Prague: Institute of Theoretical and Applied Mechanics of the Czech Academy of Sciences, 2018, pp. 745–748. ISBN: 978-80-86246-88-8.
- [138] GAO, X., T. ZHANG, J. ZHOU, S. M. GRAHAM, M. HAYDEN and Ch. ROE. On stress-state dependent plasticity modeling: Significance of the hydrostatic stress, the third invariant of stress deviator and the non-associated flow rule. *International Journal of Plasticity*, 2011, **27**(2), 217–231.
- [139] ŠEBEK, F., P. KUBÍK, J. PETRUŠKA and J. ZAPLETAL. Non-associated flow rule in the prediction of complex stress states and deformations. In *Experimental Stress Analysis 2019*. Brno: Czech Society for Mechanics, 2019, pp. 488–492. ISBN 978-80-214-5766-9.

- 
- [140] NGUYEN, V.-D., T. PARDOEN and L. NOELS. A nonlocal approach of ductile failure incorporating void growth, internal necking, and shear dominated coalescence mechanisms. *Journal of the Mechanics and Physics of Solids*. 2020, **137**, 103891.
- [141] HAIGH, B. P. The strain-energy function and the elastic-limit. In *Report of the Eighty-Seventh Meeting of the British Association for the Advancement of Science, Bournemouth: 1919*. London: John Murray, 1920, pp. 486–495.
- [142] WESTERGAARD, H. M. On the resistance of ductile materials to combined stresses in two or three directions perpendicular to one another. *Journal of the Franklin Institute*. 1920, **189**(5), 627–640.

# A Stress state characterization

A geometrical representation may be realized within the Cartesian coordinate system of principal stresses not ordered according to the magnitude ( $\sigma_I, \sigma_{II}, \sigma_{III}$ ) – the Haigh–Westergaard space [141, 142]. The space cannot be formed with principal stresses ordered according to the magnitude as for example  $\sigma_1 = \sigma_2 = 0$  MPa and  $\sigma_3 = 1$  MPa is inadmissible. Otherwise, only two octants would be needed. The Cartesian coordinate system is illustrated together with cylindrical ( $r, \theta_L, z$ ) and spherical ( $\varrho, \theta_L, \varphi$ ) coordinate systems in Fig. A.1, where  $z$  is the axial coordinate,  $\varrho$  is the radial coordinate of spherical coordinate system and  $\varphi$  is the polar angle according to

$$\varphi = \operatorname{arccot} \left( \frac{3}{\sqrt{2}} \eta \right). \quad (\text{A.1})$$

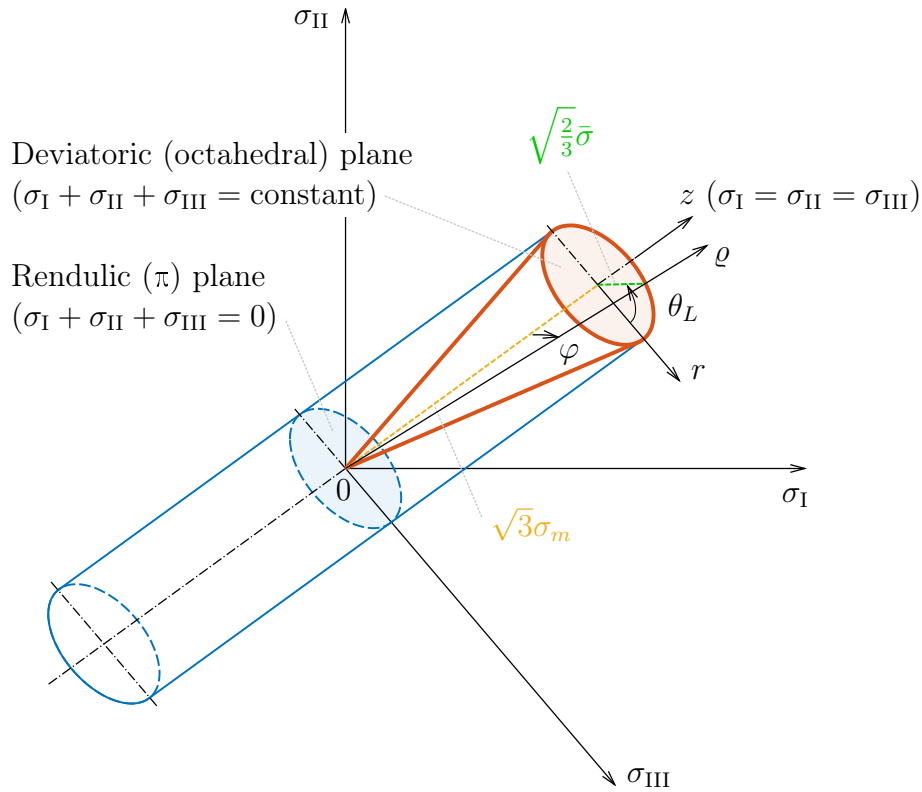


Figure A.1: Geometrical representation of the stress state

The deviatoric or octahedral plane is any plane perpendicular to the axis of the first and seventh octants (perpendicular to the hydrostatic axis where  $\sigma_I = \sigma_{II} = \sigma_{III}$ ). A special case of such a plane is Rendulic or  $\pi$  plane, which above the perpendicularity to the hydrostatic axis also contains the origin of Haigh–Westergaard space (Fig. A.1).

There are other deviatoric state variables apart from the normalized third invariant of deviatoric stress tensor and Lode angle. The one very close to Lode angle  $\theta_L$ <sup>5</sup> is the azimuth angle ranging  $-\pi/6 \leq \theta_A \leq \pi/6$  defined as

$$\theta_A = \theta_L - \frac{\pi}{6}. \quad (\text{A.2})$$

The azimuth angle can be normalized as

$$\bar{\theta} = -\frac{6}{\pi}\theta_A, \quad (\text{A.3})$$

so the range is  $-1 \leq \bar{\theta} \leq 1$ . Then, the Lode parameter has the same range as the normalized Lode angle  $\bar{\theta}$ ,  $-1 \leq L \leq 1$ , with the following definition

$$L = \sqrt{3} \tan\left(-\frac{\pi}{6}\bar{\theta}\right). \quad (\text{A.4})$$

Finally, all the deviatoric stress state measures are graphically represented in Fig. A.2 under the condition of plane stress.

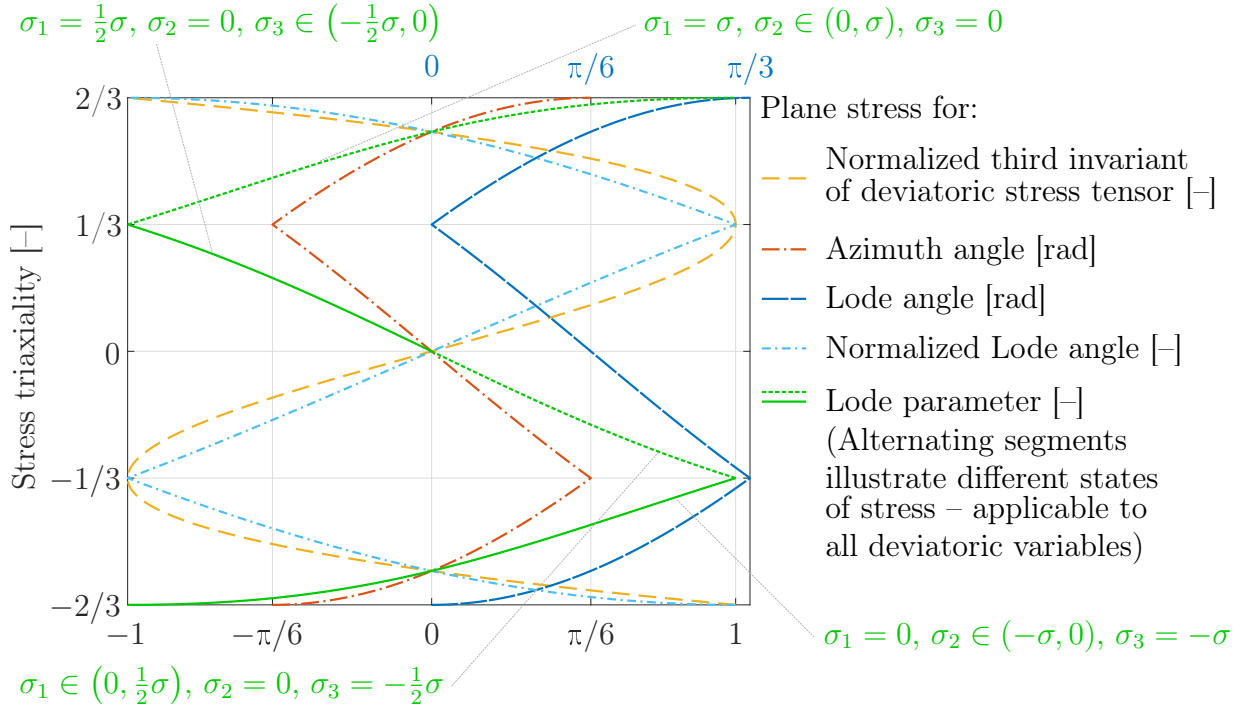


Figure A.2: Graphical representation of the deviatoric stress state measures

<sup>5</sup> Lode angle is defined with the help of the normalized third invariant of deviatoric stress tensor in Eq. 1.31.